Journal of Structural Geology, Vol. 14, No. 1, pp. 85 to 104, 1992
Printed in Great Britain

0191-8141/92 $05.00+0.00

Single layer buckle folding in non-linear materials—I. Experimental study of fold development from an isolated initial perturbation

MOHAMMAD R. ABBASSI and NEIL S. MANCKTELOW

Geologisches Institut, ETH-Zentrum, CH-8092 Zürich, Switzerland

(*Received* 27 *September* 1990; *accepted in revised form* 23 *May* 1991)

Abstract—Scale-model experiments, involving pure shear compression of a single layer embedded in a weaker matrix, were carried out to study the influence of a pre-existing isolated perturbation in the shape of an otherwise planar layer on the location and shape of folds. Different grades of paraffin wax were used as analogues for rocks with power-law rheology. The wax used for the matrix flows in steady state with a stress exponent of about 3.8. The layer has a stress exponent of about 3 and strain softens. Viscosity ratios (considered at yield stress for the layer and matrix) of 30:1 and 8:1 were used. Bell-shaped perturbations were introduced into the layer with initial average wavelengths of 8, 16 and 32 times layer thickness and corresponding initial limb dips of 12°, 5° and 3° respectively. The fold packet develops at the site of the introduced perturbation and spreads slowly along the layer with increasing shortening. The shape of the initial perturbation strongly influences the fold geometry: broader initial perturbations develop broader folds, undergo more layer parallel shortening and develop a wider zone of contact strain. The influence of the introduced perturbation shape is most marked when its average wavelength component is larger than the dominant wavelength (i.e. the wavelength of maximum growth rate). The degree of bonding between layer and matrix also influences fold development. Folds with welded layer–matrix boundaries amplify much more slowly, with a greater proportion of layer parallel shortening, than folds where slip between layer and matrix is promoted.

INTRODUCTION

BUCKLE folds, which develop due to the mechanical instability of layered or anisotropic rocks under compression, produce some of the most spectacular examples of deformation structures on scales that range from millimetres to kilometres. The simplest example of buckle fold development, which also occurs quite commonly in nature, is that of an isolated single layer embedded in a weaker matrix (e.g. Sherwin & Chapple 1968, Hudleston & Holst 1984). In this case, the spacing of layers is sufficiently large that folding can develop independently within each individual layer, leading to an overall disharmonic fold pattern. Establishing the parameters which control folding in this simple system represents a first step towards investigating more complex geometries involving multiple layers.

A large body of both theoretical and experimental work already exists on the development of single layer buckle folds (e.g. Biot 1961, 1965, Biot *et al.* 1961, Ramberg 1961, 1963, 1964, Hudleston 1973, Fletcher 1974, Cobbold 1975, Smith 1975, Neurath & Smith 1982). As with all instabilities, a small perturbation in the basic flow, usually due to some initial irregularity in the layer, is required to initiate buckle folding (e.g. Biot *et al.* 1961, Cobbold 1975). Folding of a single layer can only develop a regular wavelength, independent of the shape and location of the initial layer irregularities, if the total amplification of the dominant (i.e. the fastest growing) wavelength component is large enough to effectively swamp these initial irregularities. As extensively discussed by Biot (1961) and Biot *et al.* (1961), buckling theory suggests that the total amplification required should be greater than about 1000. It is easily shown (see Appendix) that such a large amplification can only be achieved during the low-limb dip stage of fold formation, when the wavelength is established (Chapple 1968), if the initial irregularities are very small indeed. For example, the initial amplitude of the irregularities would need to be <0.004 mm in a 1 cm thick layer. Such extremely smooth layers are unlikely in nature and the amplification of folds will generally be much less than 1000 when wavelength selection effectively ceases. Values of natural fold amplification in the range 10–40 may be more realistic (e.g. Hudleston & Holst 1984). The shape and distribution of initial perturbations along the layer will thus have a strong influence on the location and shape of folds, as has been suggested from earlier analogue experiments (Willis 1893, Cobbold 1975, Abbassi & Mancktelow 1990) and from numerical simulations (Lewis & Williams 1978, Williams *et al.* 1978). Natural fold trains show a corresponding substantial degree of irregularity and are often only approximately periodic (Sherwin & Chapple 1968, Fletcher & Sherwin 1978, Hudleston & Holst 1984, Ramsay & Huber 1987, figs. 17.7, 19.3, 19.7 and 19.23, Abbassi & Mancktelow 1990).

The aim of this work is to investigate experimentally the relationship between initial perturbation shape and fold geometry at finite amplitude, extending the earlier study of Cobbold (1975). The influence of the degree of bonding between layer and matrix and of the viscosity contrast between layer and matrix is also considered. Fourier analysis of fold shape is used to establish the growth rate of the various wavelength components. The sum of these wavelength components represents the shape of the non-periodic folds developed serially from a single perturbation. A major advantage of analogue

scale-model experiments is that the geometry of developing deformation structures can be continually observed to finite amplitudes, similar to those of natural structures. With the aid of an inscribed grid, a digitizing tablet and a small personal computer, the flow related to development of such structures can be analysed in considerable detail (Mancktelow 1991). Analogue materials can be chosen which show non-linear rheological behaviour similar to that currently believed to be most applicable for large-strain deformation in rocks. For this study, different grades of paraffin wax are used for layer and matrix to model folding in rocks with power-law rheology (Cobbold 1975, Neurath & Smith 1982, Mancktelow 1988b). Part II of this paper (Mancktelow & Abbassi 1992) uses the experimental results presented here to make direct comparison with current theories on buckle folding in non-linear materials.

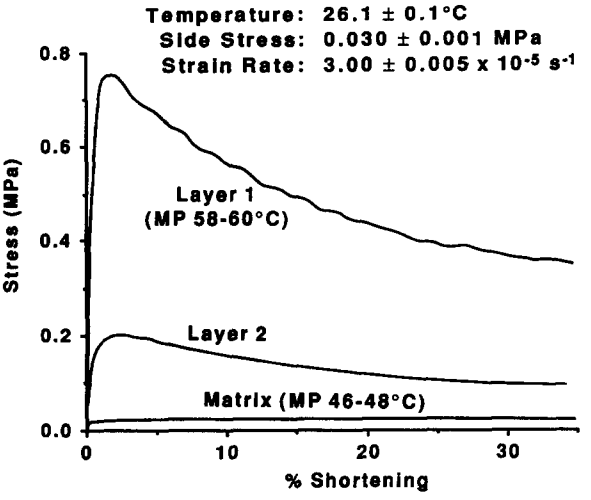

Fig. 1. Stress–strain calibration curves for the matrix (paraffin wax of melting range 46–48°C), the stiffer layer (Layer 1: paraffin wax of melting range 58–60°C) with yield stress *ca* 30 times the flow stress of the matrix, and for the less stiff layer (Layer 2: a mixture of these two waxes) with a yield stress *ca* 8 times the flow stress of the matrix. Calibration conditions are the same as experimental conditions for the scale models.

METHOD

Experimental conditions and material properties

All experiments were performed in pure shear using the automated deformation rig described in detail in Mancktelow (1988a). The strain-rate was maintained at $3.00 \times 10^{-5}\,s^{-1}$, the stress σ_3 on the confining plates at 3×10^4 Pa (0.3 bar), and the temperature at 26.1 ± 0.1°C. The experiments were photographed at regular intervals, using a high quality, large format camera to minimize distortion. Photographic enlargements were used for measurement of the fold parameters described here and the nodal points of the inscribed grid digitized for further analysis of the strain and displacement fields (Mancktelow 1991).

Two grades of paraffin wax were employed as model materials: the weaker matrix has a melting range of 46–48°C and the stiffer layer 58–60°C. Details of the properties of paraffin wax and of the suppliers can be found in Mancktelow (1988b). For the given experimental conditions, the paraffin waxes were within their β field and have an elastic–non-linear viscous rheology (Figs. 1–4), with a power-law relationship between differential flow stress σ and strain rate $\dot{\varepsilon}$ (Cobbold 1975, Mancktelow 1988b) of the form:

$$\dot{\varepsilon} = B \exp\left(\frac{-Q}{RT}\right) \sigma^n \varepsilon^\kappa,$$

where B is a material constant, Q the activation energy, R the gas constant, T the absolute temperature, n the stress exponent and κ the strain sensitivity (reflecting any tendency to strain soften or harden). The matrix flows in steady-state (i.e. $\kappa = 0$, Fig. 1), with a stress exponent n of about 3.8 (Fig. 2). Note that this is significantly higher than the calibrated value of 2.7 given in Mancktelow (1988b) for the same grade of paraffin wax (melting range 46–48°C) and reflects the unfortunate observation, as noted in that paper, that different batches from the same supplier can exhibit slightly different rheologies. It is imperative, therefore, to calibrate each batch under the same conditions as the experiments in question. The paraffin wax of melting range 58–60°C, used to construct the stiff layer, exhibits strong strain softening behaviour (Layer 1 in Fig. 1). For the range of strain relevant to the current experiments ($\varepsilon < 0.2$), the strain sensitivity $\kappa \approx 3$ (Fig. 3), and the stress exponent is also around 3 (Fig. 4). Phenomenologically, the material is ductile, without any sudden stress drop associated with a through-going fault surface. In detail, however, the deformation occurs at least in part along numerous small dilatant fault surfaces. As developed theoretically by Neurath & Smith (1982), the effect of strain softening may be considered, to a first-

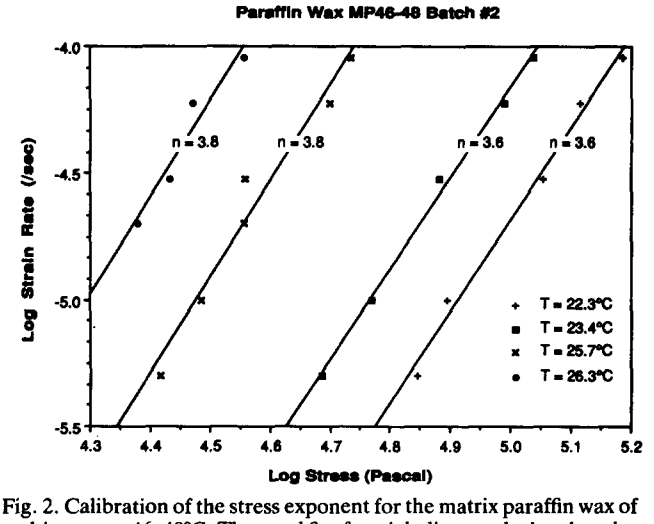

Fig. 2. Calibration of the stress exponent for the matrix paraffin wax of melting range 46–48°C. The good fit of straight lines to the log–log plot demonstrates that the power-law relationship between strain rate and stress is a reasonable approximation to the rheology of this material. Note that the value of 3.8 is considerably higher than the value of 2.7 obtained on a previous batch of the same grade of wax from the same supplier (Mancktelow 1988b), underlining the need to independently calibrate each batch under experimental conditions.

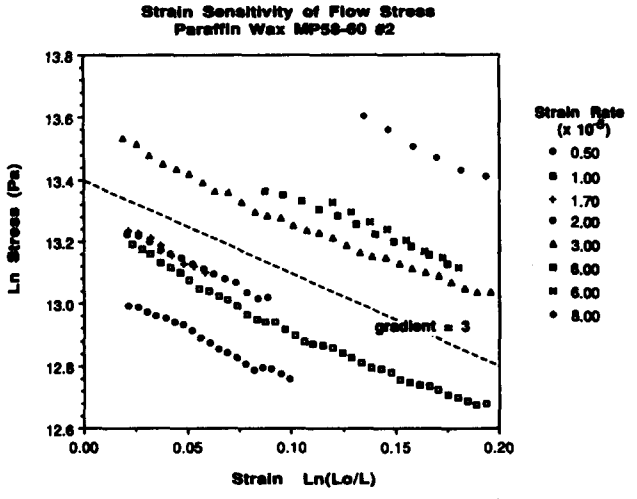

Fig. 3. Strain softening behaviour of the paraffin wax of melting range 58–60°C used to construct the stiff layer (Layer 1). The linearity of this ln–ln plot is good at the low values of bulk shortening of interest in our fold analysis. At higher bulk strains, beyond the range of the current plot, the curves tend towards flatter slopes. All calibrations at a temperature of 26.1 ± 0.1°C.

order approximation, as equivalent to an increase in the effective power-law stress exponent, with the magnitude of this increase depending on the fold growth rate (see Part II, Mancktelow & Abbassi 1992).

The strain softening behaviour of the layer results in a decreasing viscosity ratio between layer and matrix with increasing strain (Fig. 1). The maximum value, as given by the ratio between the yield stress of the stiffer layer and the steady state flow stress of the matrix, is around 30:1 (Layer 1 in Fig. 1). One experiment was also performed in which the layer was a mixture of the 46–48°C and 58–60°C waxes, such that the maximum viscosity contrast between layer and matrix was only 8:1 (Layer 2 in Fig. 1). This additional experiment allows a limited discussion on the influence of viscosity ratio on fold development.

For most experiments, the matrix and layer of the models were constructed independently (see below for details), such that cohesion between layer and matrix was minimized, approximating the 'easy-slip' condition generally assumed by Biot (e.g. Biot 1961). The confining stress σ_3, applied to the side plates of the pure shear rig during deformation (Mancktelow 1988a), suppressed any tendency for separation between layer and matrix. A series of experiments were also carried out, in which the layer was poured as molten wax into a mould constructed of the already pre-shaped matrix. This produced strong cohesion between matrix and layer (cf. Cobbold 1975) and allowed an experimental investigation of the influence of degree of bonding between matrix and layer, as discussed in detail below.

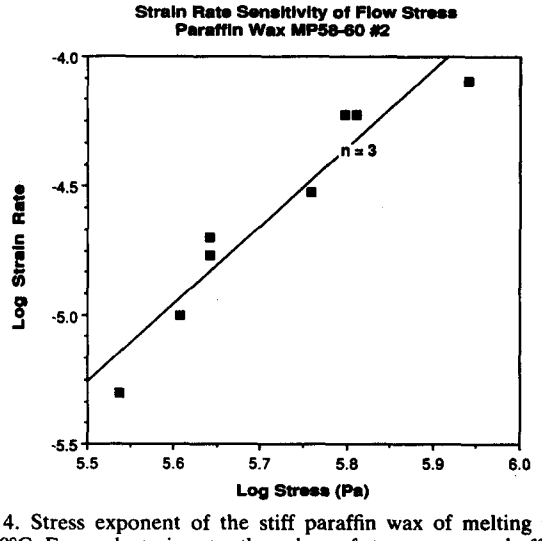

Fig. 4. Stress exponent of the stiff paraffin wax of melting range 58–60°C. For each strain rate, the values of stress were read off from Fig. 3 at a standard strain state (natural strain ln $(L_0/L) = 0.10$). The plot is approximately linear, with a stress exponent of *ca* 3, which is not significantly different from the calibrated stress exponent for the matrix wax.

Geometry of the initial perturbation

Symmetric perturbations were introduced as bell-shaped forms corresponding to the equation

$$y(x) = \frac{b}{1 + \left(\frac{x}{a}\right)^2}$$

(cf. Biot *et al.* 1961) (Fig. 5). The amplitude b, measured

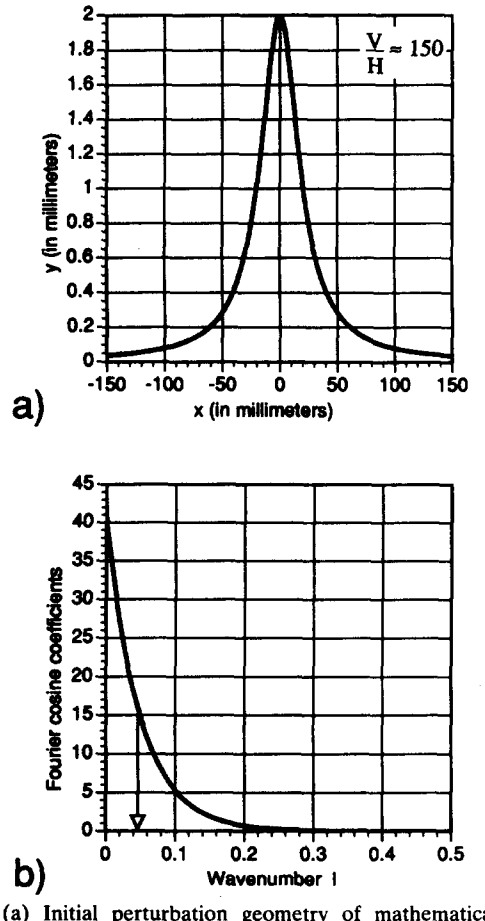

Fig. 5. (a) Initial perturbation geometry of mathematical form $y(x) = b/[1 + (x/a)^2]$. The example given is for Pert C, with $b = 2$ mm and $a = 20.37$, giving an average wavelength to the perturbation of 128 mm, i.e. 32 times layer thickness for a 4 mm thick layer. Vertical scale is strongly exaggerated (150:1). (b) Cosine coefficients for the infinite Fourier series representing the curve in (a). The arrow points to the average wavenumber ($l_{av} = 0.049$), which is taken to occur where the curve drops to 1/e of its maximum value.

at the central symmetry axis (where $x = 0$), was set at 2 mm, and the layer thickness was maintained at around 4 mm, such that the initial amplitude of the perturbation was always approximately half the layer thickness. The value of a controls the width of the bell-shape, and consequently also the position of maximum slope of the curve, which occurs at $x = \pm(\sqrt{3}/3)a$, with values of $\pm(3\sqrt{3}/8)b/a$. Three values of a were used in our experiments (a = 5.09, 10.19 and 20.37 mm), corresponding to narrow (Pert A), intermediate (Pert B) and broad (Pert C) initial perturbations, with theoretical maximum limb dips of 14.3°, 7.3° and 3.6°, respectively. These initial maximum dip values occur at only a single point along each curve and are clearly not directly measurable from the photographs: the values measured from the models and used in the analysis below were somewhat lower, with values of 12°, 5° and 3°, respectively.

In practice, moulds were first constructed with the correct mathematical shape using a numerically driven milling machine. Plaster of Paris was poured into these moulds to construct layers of the required thickness, and then impregnated with a fine epoxy spray to produce an impermeable non-stick surface. The layers were then slotted into rectangular moulds into which the molten wax for the matrix block was poured. For most experiments (the easy-slip experiments, see above), the layer was produced by planing of a separate block of higher melting point wax. The planar layer was then warmed and gently formed into the correct shape between the moulds used initially to construct the plaster layer. Layer and matrix could then be placed together during planing of the whole block to its correct dimensions and for inscription of the grid (cf. Mancktelow 1988a). For the experiments where good bonding between layer and matrix was required, the steps were similar except that molten wax for the layer was poured directly into the space left by the plaster layer within the matrix block.

Several experiments were repeated to check reproducibility and these carry an additional identification number (e.g. Pert C1). Initial model dimensions were always *ca* 29 cm long × 12 cm wide × 6 cm thick. Several additional experiments in which symmetric and asymmetric initial perturbations were compared have already been reported in Abbassi & Mancktelow (1990).

Fourier analysis

The initial perturbation introduced into the single layer is not sinusoidal and, therefore, does not have a single wavelength or amplitude. A distinction must be made between the 'amplitude' of the central non-sinusoidal 'fold' as measured from the photographs (e.g. Figs. 6–8) and the amplitude of the various sinusoidal components which can represent this isolated fold shape. The introduced bell-shaped curve can be written as a Fourier integral:

$$\frac{b}{1+\left(\frac{x}{a}\right)^2} = ab\int_0^\infty e^{-al}\cos lx\, dl.$$

If the wavenumber l is defined as $l = 2\pi/L$, where L is the wavelength, then the 'average wavenumber' of the perturbation is given by $l_{av} = 1/a$ (Biot *et al.* 1961). In the Fourier representation, this is the wavenumber for which the amplitude of the cosine component is 1/e of the maximum value (i.e. ab/e, where e = 2.7183, the natural log base). This implies that the average wavelength is $L_{av} = 2\pi a$. The selected initial perturbation shapes Pert A, B and C have L_{av} values of 8, 16 and 32 times layer thickness, respectively.

For discretely sampled data, as in the case of our digitized fold, the continuous and infinite Fourier integral can be approximated by a discrete finite series of sine and cosine coefficients (cf. Mancktelow & Abbassi 1992). For an even function, such as the bell-shaped curve, all sine coefficients should be zero. Due to imperfections in preparation, however, there are always some non-zero sine coefficients in the starting shape. During deformation, individual Fourier coefficients grow at differing rates, allowing the construction of a curve for growth rate vs wavelength (or more conveniently, layer thickness/wavelength). The form of this curve depends on the material properties, and can be directly compared with results from current theories for buckle folding in non-linear materials (Mancktelow & Abbassi 1992).

Measurement of layer parallel shortening

As expected for the relatively low viscosity contrasts employed in our experiments, there is significant shortening and thickening of the layer during fold development. To analyse this process, the layer parallel shortening was determined by first fitting a tight cubic spline to the digitized central line of the fold to minimize the effect of digitizing error (Panozzo 1988), and then summing along this line for the full length of the layer to obtain the arc length. The layer parallel shortening is then given by:

$$\%\ \text{layer parallel shortening} = \frac{\text{initial arc length} - \text{current arc length}}{\text{initial arc length}} \times 100.$$

This is clearly an average value along the full length of the layer. As folds develop to finite amplitude, however, the distribution of layer parallel shortening along the layer may become markedly heterogeneous, leading to hinge thickening and limb thinning and the development of 'flattened parallel folds' (e.g. Ramsay 1967, p. 411).

EXPERIMENTAL RESULTS

Influence of the span width of the initial perturbation

Folding and fracture. Shortening of 40% can easily be achieved in the deformation rig employed, but for the higher viscosity contrast experiments (viscosity ratio ≈30), extension cracks invariably develop on the outer arcs of folds when the radius of curvature attains values

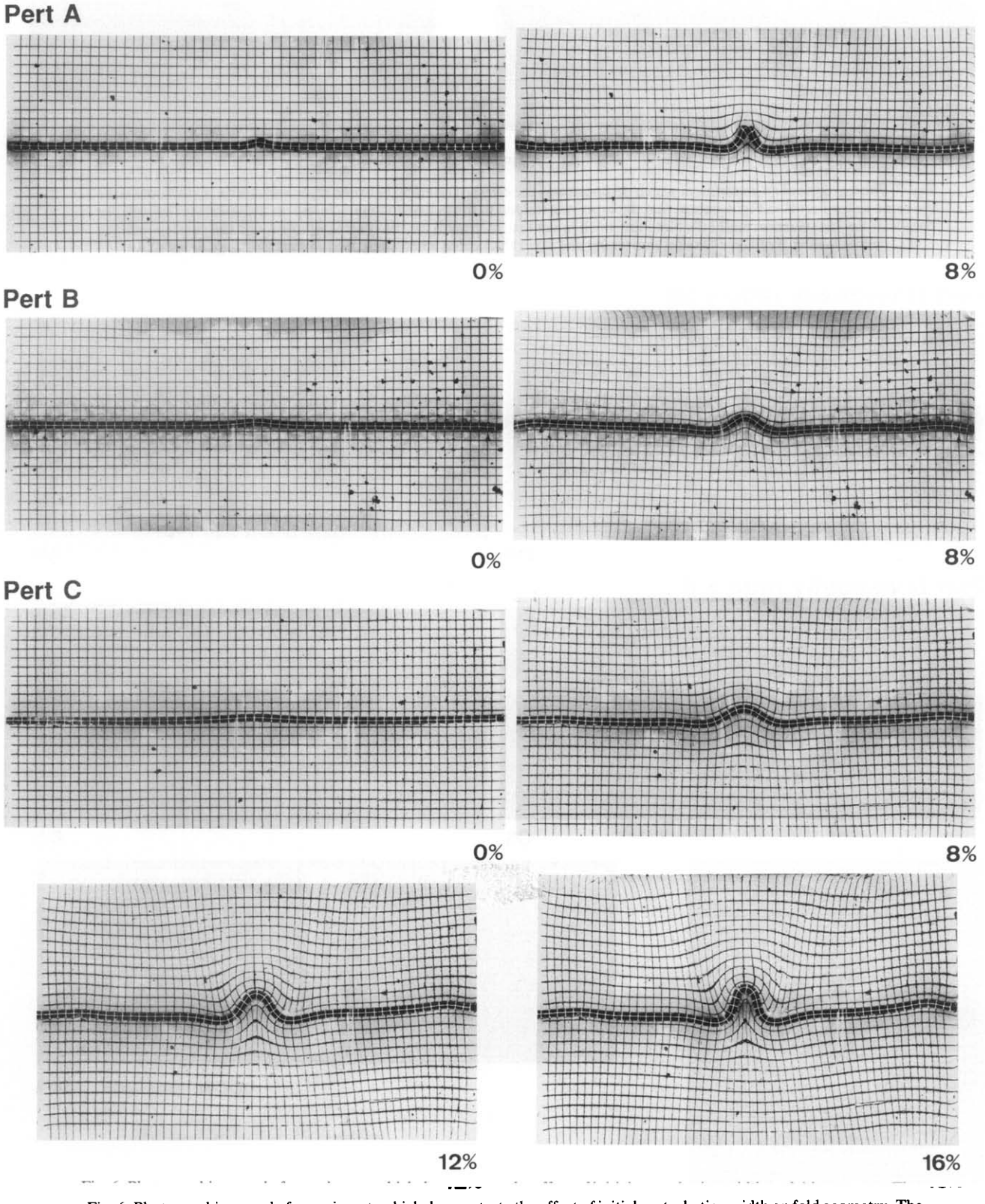

Fig. 6. Photographic record of experiments which demonstrate the effect of initial perturbation width on fold geometry. The layer thickness was in each case *ca* 4 mm and the viscosity ratio between layer and matrix 30:1. The interface between layer and matrix was unwelded, promoting easy slip. Values of bulk shortening are indicated below each photograph.

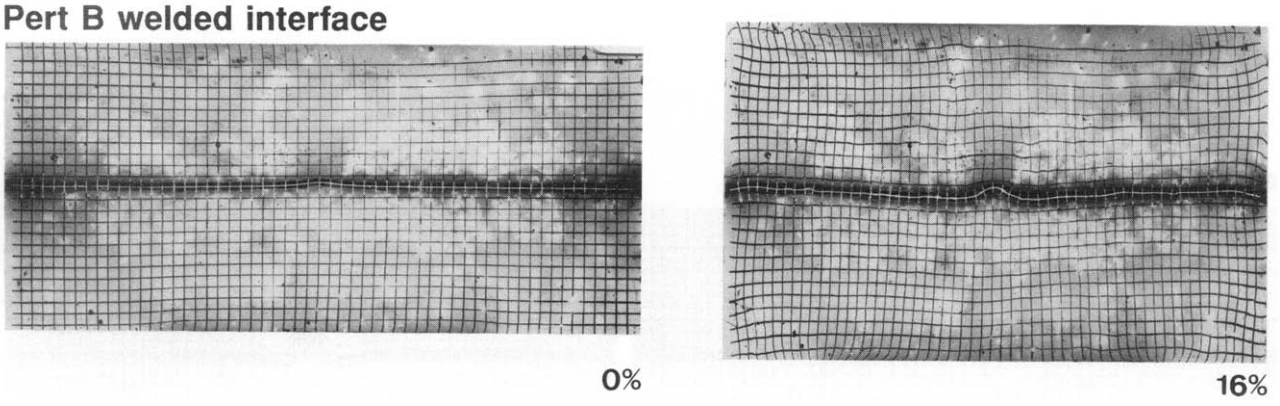

Fig. 7. Photographs of an experiment which demonstrates the effect of bonding between layer and matrix. Conditions were the same as for Pert B in Fig. 6 except that the layer was welded to the matrix to minimize slip on the interface (see text for details of the construction method). Note the much lower rate of growth for the central antiform and the correspondingly greater amount of layer parallel shortening and layer thickening when compared to Pert B in Figs. 6 and 9.

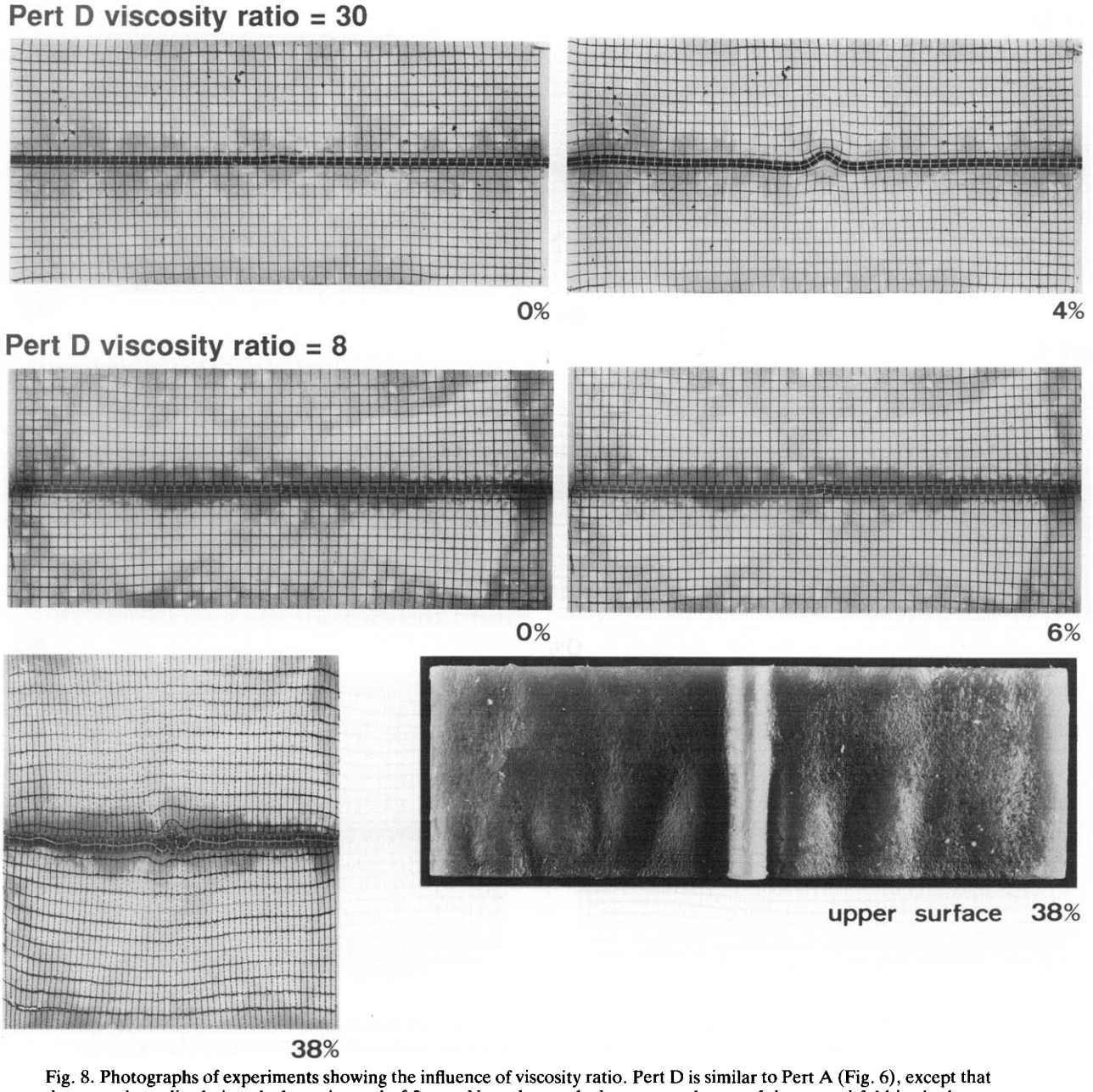

Fig. 8. Photographs of experiments showing the influence of viscosity ratio. Pert D is similar to Pert A (Fig. 6), except that the central amplitude is only 1 mm instead of 2 mm. Note the much slower growth rate of the central fold in the lower viscosity ratio experiment, the greater layer parallel shortening and thickening and the much reduced zone of contact strain. The two lower photographs were taken at the same percentage bulk shortening: that to the right shows the surface of the layer looking down on the folded layer from above. Note the subsidiary non-cylindrical folds developed away from the central perturbation.

less than about 1.2 times the layer thickness. Fracture initiation occurred at around 5% bulk shortening for Pert A, 8% shortening for Pert B and 16% shortening for Pert C. This effect largely reflects the difference in the initial radius of curvature of the introduced perturbations: broader perturbations (e.g. Pert C) shorten more before the critical value of 1.2 is overstepped. Layer parallel shortening, which is more pronounced for the broader perturbations (see below), may also have an important influence. Layer parallel shortening tends to counteract the tendency for extension on the outer arc of buckle folds (cf. figs. 21.25 and 21.26 from Ramsay & Huber 1987) and, therefore, to suppress the development of extensional cracks. This effect is even more strongly developed for low viscosity contrast between matrix and layer: the experiment with viscosity ratio of only 8:1 underwent 38% shortening without failure (Figs. 8 and 23). Similarly, in the experiment with a viscosity contrast of 30:1 but with welded layer–matrix contacts, significant layer parallel shortening was observed, and 38% bulk shortening was again possible without failure (Figs. 7 and 19).

Fold location and shape. As is clear from Figs. 6–9, the presence of an initial perturbation determines the location of the developing fold and exerts a strong influence on the fold shape. A narrower initial perturbation results in a narrower final fold shape. This effect is seen particularly clearly from plots of the cosine coefficients of the Fourier series representing each fold shape (Fig. 13). Although the material properties and strain geometry are the same in each case, the position of the

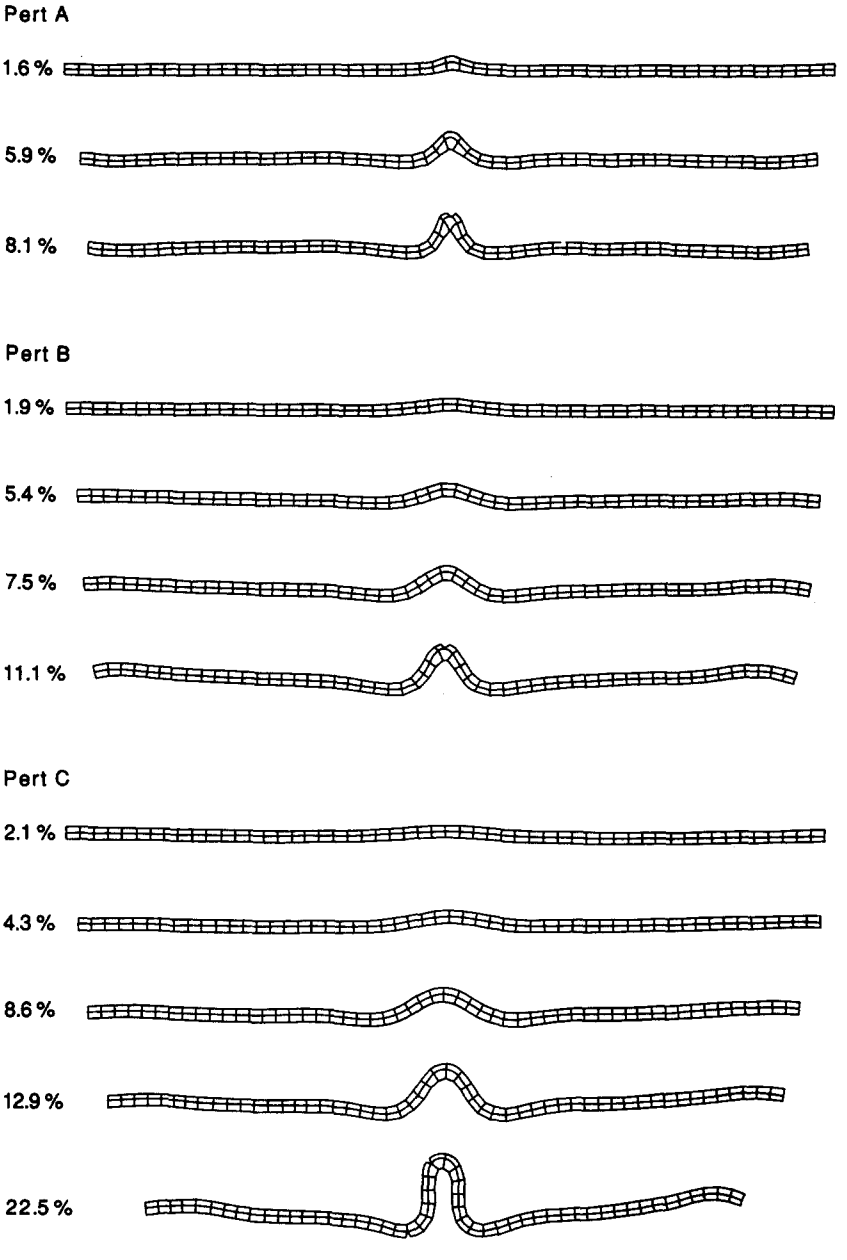

Fig. 9. Fold geometry developed in single layers from initial perturbations of three different span widths. For Pert A, the average wavelength to layer thickness value was 8; for Pert B, 16; and for Pert C, 32. The layer thickness in each case was *ca* 4 mm, the central amplitude of the perturbation, *ca* 2 mm, and the viscosity ratio between matrix and layer, 30:1.

component of maximum amplitude is different for each initial perturbation: for a narrower perturbation (e.g. Pert A) it always occurs at a shorter wavelength than for a broader perturbation (e.g. Pert C), reflecting the influence of the initial perturbation shape even to large finite amplitudes.

Fold amplitude and limb dip. The amplitude of the central antiform (normalized against the initial amplitude A_0) is presented for each of the three initial perturbation shapes in Fig. 10(a), together with the amplitude of the flanking synforms which develop during the experiments. If the natural logarithm of the normalized amplitude is plotted against logarithmic strain, then the slope at a specific strain will represent the instantaneous growth rate (cf. Smith 1979, Neurath & Smith 1982). The results are presented in Fig. 10(b), where it is seen that the growth rate is at least approximately constant at low bulk shortening ($\varepsilon < ca$ 0.08), but then decreases. For the same bulk shortening, the amplitude of the central antiform for the narrow perturbation Pert A is always greater than for Pert B and C and this is reflected in the growth rates: Pert A has a growth rate of *ca* 25,

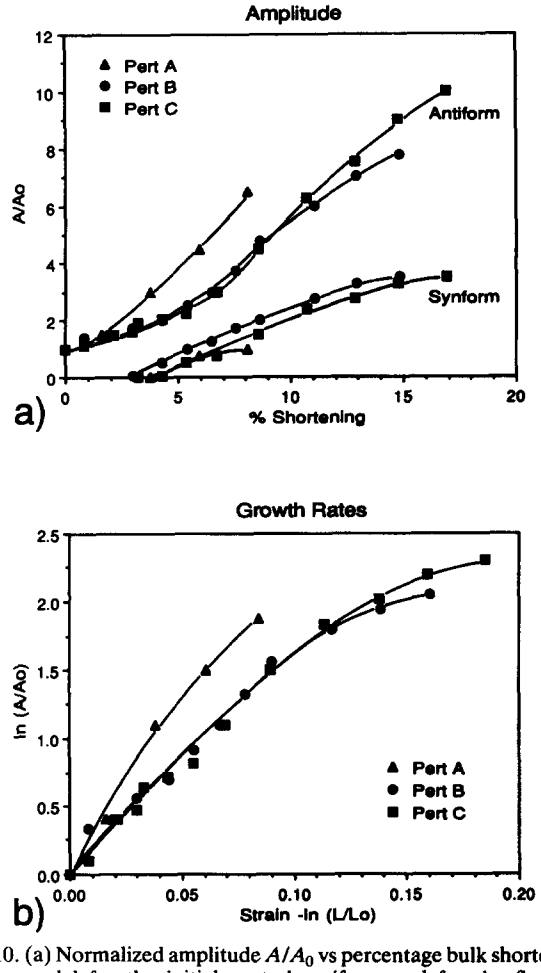

Fig. 10. (a) Normalized amplitude A/A_0 vs percentage bulk shortening of the model for the initial central antiform and for the flanking synforms which develop during progressive folding, where A_0 is the initial amplitude of the perturbation. (b) ln (A/A_0) vs ln (L_0/L), i.e. $-\varepsilon$, the natural or logarithmic strain. The slope of such a curve gives the 'growth rate' of the fold at any specific strain (cf. Neurath & Smith 1982, Abbassi & Mancktelow 1990). Pert A has an initial growth rate of *ca* 25, whereas Pert B and Pert C both have growth rates of *ca* 16.

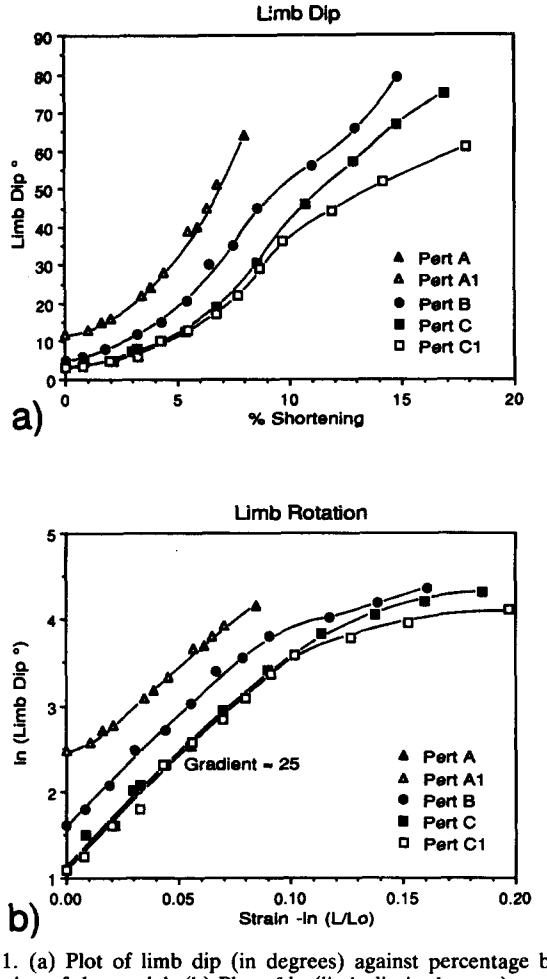

Fig. 11. (a) Plot of limb dip (in degrees) against percentage bulk shortening of the model. (b) Plot of ln (limb dip in degrees) against ln (L_0/L).

whereas Pert B and C have similar growth rates of around 16.

Similar plots to those for amplitude and amplitude growth rate can be constructed for the limb dip and rate of limb rotation (Fig. 11). Because the different initial perturbations have different initial limb dips, the curves are displaced relative to each other, but the initial rotation rates are basically identical with a value around 25. Duplicate experiments (Pert A1 and C1) in Fig. 11 demonstrate the excellent reproducibility of the results. The similarity in form of Figs. 10(a) and 11(a) suggests a simple relationship between normalized amplitude and limb dip: the plot in Fig. 12 confirms this and shows that it is effectively linear.

As noted earlier, a distinction should be made between the amplitude of the fold developed from the initial isolated perturbation, which is not a regular periodic structure with a single wavelength, and the amplitude of the sinusoidal Fourier components which, on superposition, can represent the observed layer shape. The Fourier cosine coefficients for each of the initial perturbation shapes (Pert A–C), plotted against layer thickness/wavelength (h/L), are presented in Fig. 13. The distribution for the initial bell-shaped curve is exponential, decreasing towards shorter wavelengths (i.e. larger wavenumbers). This distribution is rapidly

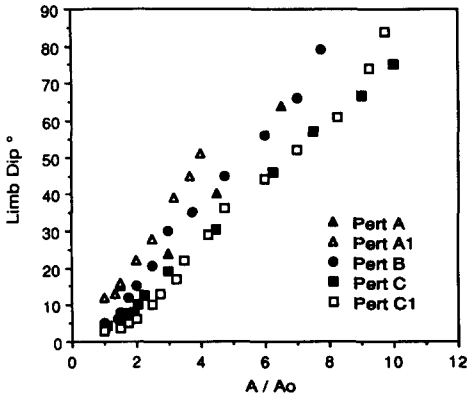

Fig. 12. Plot of limb dip vs normalized amplitude of the central fold A/A_0. The plot indicates an approximately linear relationship but with different intercepts reflecting the differing initial limb dips of the perturbations.

modified during deformation, since the rate of dynamic amplification varies with wavelength during buckling folding (e.g. Biot 1961, Biot *et al.* 1961). The growth rates of the individual Fourier cosine components derived directly from Fig. 13 are plotted in Fig. 14. The best-fit polynomial curve has a broad maximum around 0.10 for the layer thickness/wavelength, that is a dominant wavelength of around 10 times layer thickness. Neither the dominant wavelength nor the maximum growth rate are significantly influenced by the initial perturbation shape. The material properties alone (including the degree of bonding between layer and matrix, see below) determine these values, as expected theoretically (e.g. Biot 1961, Fletcher 1974).

It is important to note that the Fourier component of maximum amplitude in Fig. 13 is *not* the wavelength with the maximum growth rate (i.e. the dominant wavelength) (Fig. 14), due to the unequal distribution of amplitudes to the Fourier components in the initial perturbation shape. The growth rate of the dominant wavelength component as determined by such a Fourier analysis is considerably greater than the growth rate for the central antiformal fold as measured directly from the photographs (Fig. 10b).

Fold wavelength. It is clear from Figs. 13 and 14 that, although the dominant wavelength of maximum growth rate may remain unaltered for the various initial perturbation shapes, the wavelength component of maximum amplitude in the Fourier series is very different for Pert A, B and C. For the narrowest initial perturbation, Pert A, the maximum is initially at longer wavelength than the dominant wavelength value (i.e. lower layer thickness/wavelength values), but moves towards the dominant wavelength with increasing strain, so that for $\varepsilon = 0.083$ the component of maximum amplitude is only of slightly longer wavelength than the dominant wavelength. With increasing span of the initial perturbation (Pert B and C), the displacement of the maximum amplitude component towards longer wavelength is more and more marked, and the tendency to approach the dominant wavelength with increasing strain less pronounced. Similar results were obtained in the finite

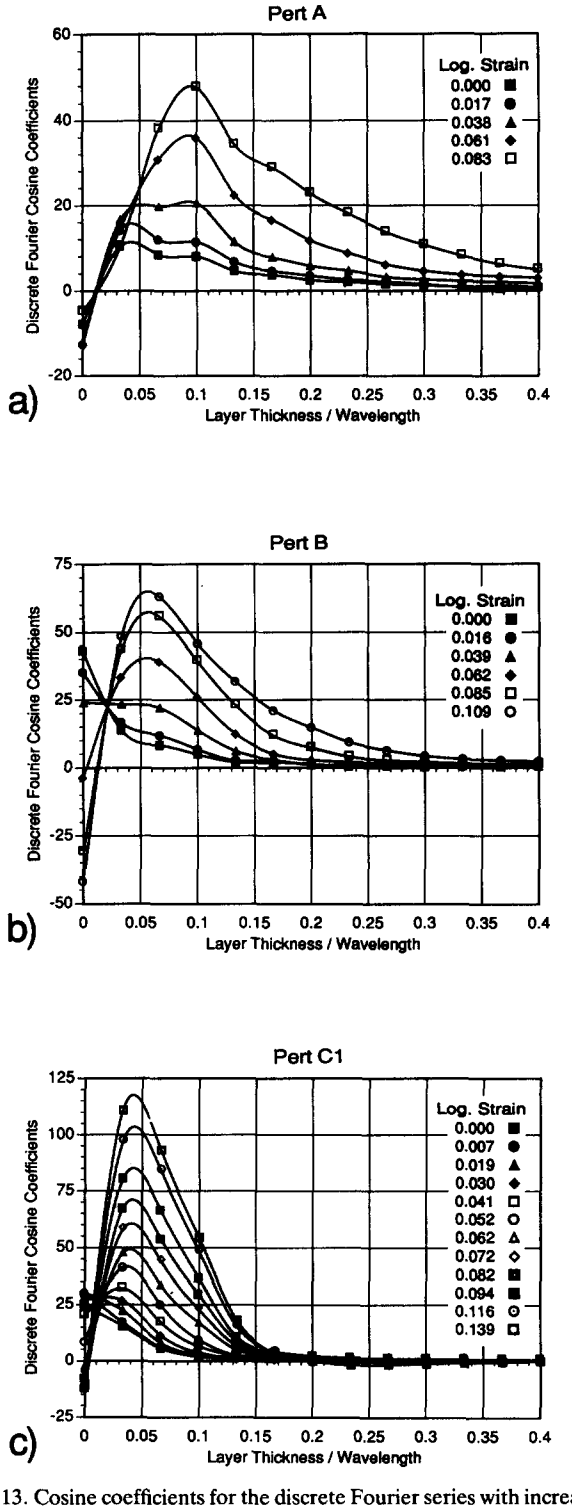

Fig. 13. Cosine coefficients for the discrete Fourier series with increasing bulk shortening. Note that a Fourier series derived from discrete data must itself be discrete, with an interval between values determined solely by the length of the digitized layer (see Appendix in Part II, Mancktelow & Abbassi 1992); it is not a continuous function. The curves through these discrete values are intended as a visual aid, linking related coefficients determined from the same fold shape at a particular bulk strain. The curves do not in themselves have any physical significance. The values of the coefficients are not normalized against the total number of data points, but as this number is the same for (a)–(c), direct comparison between the plots is still possible. (a) Results from experiment Pert A. The wavelength of maximum amplitude at $\varepsilon = 0.083$ occurs at around 11 times layer thickness, as far as interpolation between the discrete values is valid (see note above). (b) Results from experiment Pert B. The wavelength of maximum amplitude at $\varepsilon = 0.109$ occurs at around 15 times layer thickness. (c) Results from experiment Pert C1. The wavelength of maximum amplitude at $\varepsilon = 0.139$ occurs at around 22 times layer thickness.

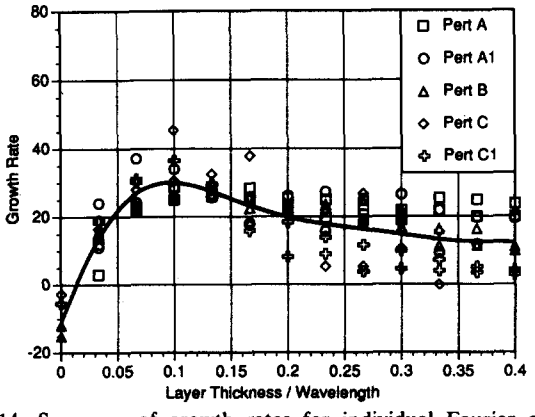

Fig. 14. Summary of growth rates for individual Fourier cosine coefficients, determined from all experiments with differing widths of the initial perturbation but the same material properties (viscosity ratio = 30:1). Growth rates are plotted against inverse normalized wavelength (thickness/wavelength = $2\pi s$, where s is normalized wavenumber). Each experiment provides two sets of results (for left and right sides of the fold). Considering the accumulated error of the several steps involved (digitization of layer shape, calculation of Fourier series, determination of growth rate of individual Fourier cosine coefficients with increasing strain by least-squares regression), the scatter in results is moderate. The scatter increases towards higher layer thickness/wavelength, largely due to increased relative errors in these very low magnitude Fourier coefficients. The solid line is a best-fit fifth-order polynomial to all the data.

element numerical models of Williams *et al.* (1978). The results confirm the observation of Biot (1961) that the establishment of a dominant wavelength independent of the initial perturbation shape requires a certain total amplification (amplification increasing with bulk shortening). The results also demonstrate that the influence of perturbation shape on the final fold shape is greatest for initial perturbations which are broad compared to the dominant wavelength (Williams *et al.* 1978).

Layer parallel shortening. Plots of the layer parallel shortening and the rate of layer parallel shortening against bulk shortening, as well as the relationship between layer parallel shortening and limb dip are presented in Fig. 15. For these parameters, the reproducibility of the repeat experiments (Pert A and A1, Pert C and C1) is again good. At low fold amplitudes and limb dips, the initial rate of layer parallel shortening with bulk shortening always approaches one (i.e. all shortening is accommodated by layer parallel shortening, cf. Ramberg 1964), irrespective of the differing perturbation geometries (Figs. 15a & b). This constant rate near 1 for the first 1–2% of bulk shortening is within the elastic range of layer and matrix (Fig. 1). With the onset of viscous flow, the rate progressively decreases until it approaches zero at around 30–40° limb dip, where all shortening is accommodated by buckling (Figs. 15b & c). Similar results were obtained for single layer fold experiments using linear viscous materials by Hudleston (1973).

Zone of contact strain. If contact is maintained between layer and matrix, folding will result in a zone of heterogeneous strain within the matrix to either side of the layer, which diminishes in magnitude with distance

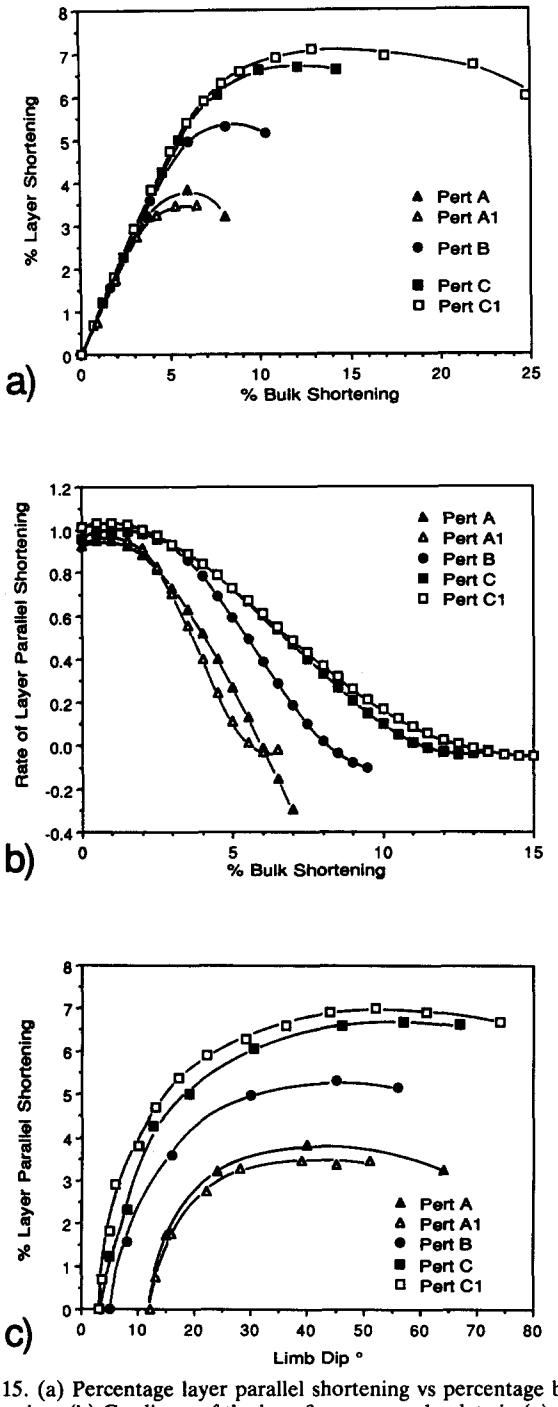

Fig. 15. (a) Percentage layer parallel shortening vs percentage bulk shortening. (b) Gradients of the best-fit curves to the data in (a), i.e. the rate of layer parallel shortening relative to bulk shortening. (c) Percentage layer parallel shortening vs limb dip in degrees.

from the layer interface (cf. the horizontal grid lines in Figs. 6–8). As noted by Ramberg (1961), this zone of contact strain can be clearly visualized by considering the additional heterogeneous displacement components over and above the background homogeneous flow. This perturbation vector displacement field can be calculated from the digitized grid nodes (Mancktelow 1991) and is presented for Pert B at 14.8% shortening in Fig. 16. The perturbation field forms closed cells with upward displacements in the core of the central antiform and compensating downward displacements to either side, leading to steadily amplifying flanking synforms

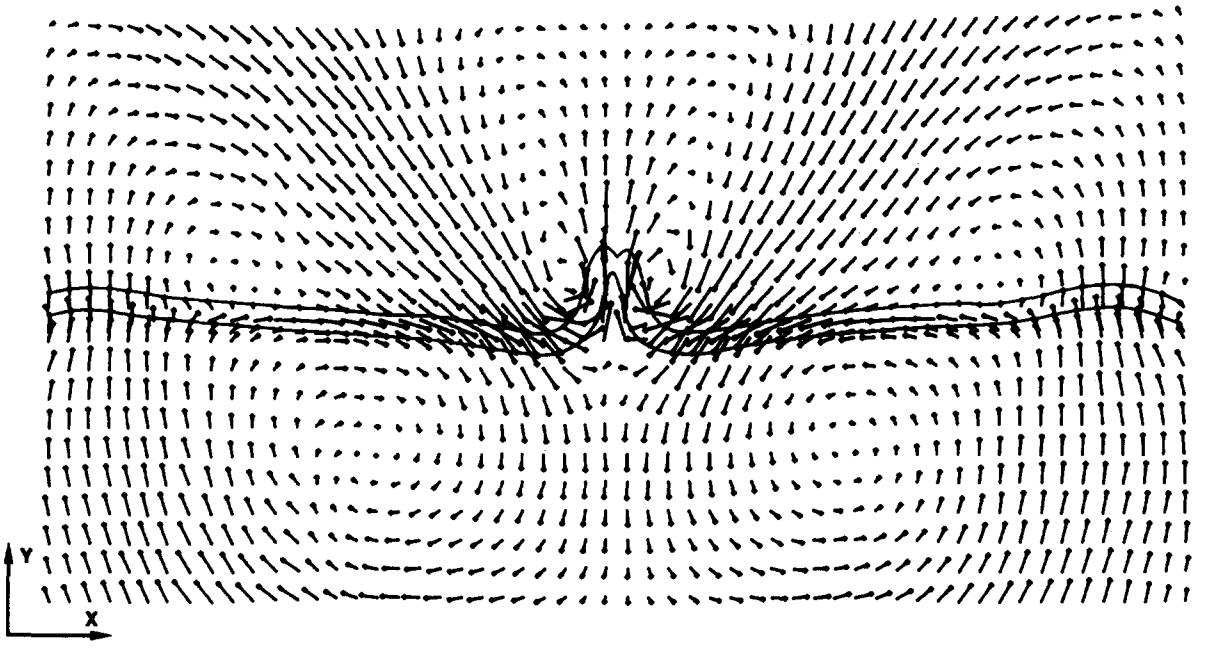

Fig. 16. Perturbation vector displacement field for Pert B at 14.8% bulk shortening, showing perturbation 'flow cells' related to the zone of contact strain developed to either side of the layer.

and thus to the sideways spread of folding along the layer (Cobbold 1975, Lewis & Williams 1978). The perturbation flow is effectively parallel to the axial plane of the symmetric central antiform at the fold hinge (Fig. 16) (Ramberg 1961). A plot of the perturbation displacement component parallel to the axial plane (i.e. the Y direction in Fig. 16), measured away from the central antiformal hinge and normalized against the value Y_0 of the layer interface itself, provides a good indication of the form and width of the contact zone (Fig. 17) (cf. fig. 3 from Ramberg 1961). It is seen from Fig. 17 that the width of the zone is dependent on the initial span of the perturbation, increasing as the breadth of the initial perturbation increases. For sinusoidal waves, Ramberg (1961) suggested that the zone of contact strain should be approximately equal to the fold wavelength. For an isolated perturbation, there is no single characteristic wavelength, but the width of the zone is approximately equal to the wavelength of maximum amplitude in the Fourier series representation (Fig. 13, for Pert A $L_{max} \approx 11$, for Pert B $L_{max} \approx 15$, and for Pert C $L_{max} \approx 22$ times layer thickness). It can be seen from Fig. 17 that, on the inner arc of the fold, the perturbation displacements in the Y direction go through negative values (i.e. displacements in the opposite direction to the fold hinge) before finally approaching zero. This effect reflects the concentration of buckle folding, and therefore shortening of the layer, about the position of the initial perturbation. This concentration of strain in a central region results in a displacement distribution as shown by the deformed grid in Fig. 18, which is superimposed on the effects due to buckling alone. The additional heterogeneous strain effect will tend to increase the displacements on the outer arc (more positive values in Fig. 17) and decrease the displacements on the inner arc, leading to a steeper curve with distance from the layer and eventually to negative values, before

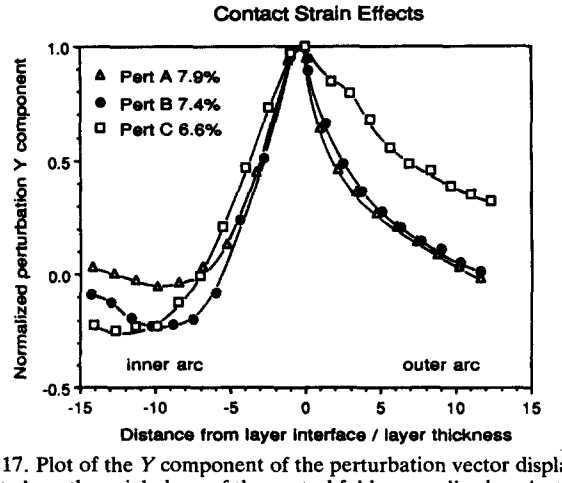

Fig. 17. Plot of the Y component of the perturbation vector displacement along the axial plane of the central fold, normalized against the value for the layer boundary, for Pert A, B and C at similar values of bulk shortening.

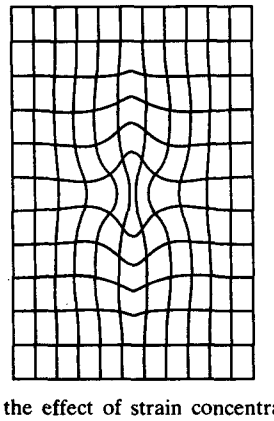

Fig. 18. Sketch of the effect of strain concentration in the central region on the shape of an originally square grid deformed under constant volume, pure shear boundary conditions.

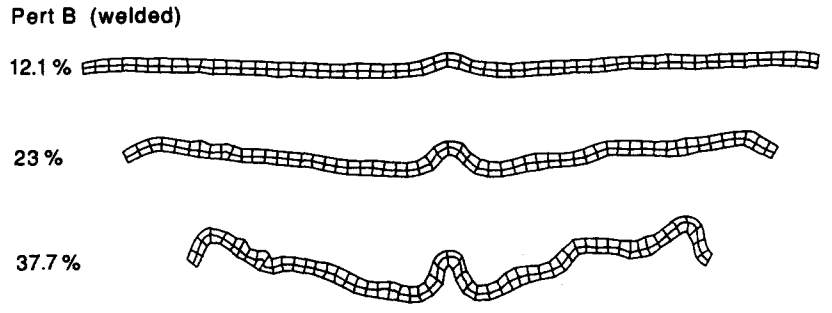

Fig. 19. Fold geometry developed in a single layer with identical experimental parameters to Pert B in Figs. 6 and 9, except that the matrix–layer interface has been welded to minimize slip.

finally approaching zero as both effects diminish towards the model boundaries.

Influence of matrix–layer bonding

The experiment with strong bonding between layer and matrix shows much slower amplification of the central perturbation and more homogeneous deformation of layer and matrix than the corresponding experiments in which bonding between layer and matrix was minimized (compare Pert B Fig. 6 with Fig. 7, also Figs. 19–21). This is reflected in the greater amount of layer parallel shortening in the layer compared to easy-slip experiments (Fig. 22). Indeed, the geometry is more similar to the low competence contrast experiment of Fig. 23 than to the easy-slip experiments with the same viscosity contrast. There is some risk that the construction method for the well bonded model may have modified the material properties of layer and adjacent matrix, such that the effective viscosity contrast was truly lower. The layer was formed by pouring molten wax into a mould formed by the already cooled matrix. As the layer was only 4 mm thick, diffusion between the initially molten layer wax and the surrounding matrix cannot be excluded. Models kept for long periods (several months), particularly at elevated temperatures, do indeed show evidence for diffusion. This is seen as a halo of the candle wax dye used to highlight the layer in the adjacent matrix: no such diffusion of the dye was observed during construction of the well-bonded model. A more difficult effect to quantify may be the influence of a possible change in microstructure of the crystalline wax in the matrix adjacent to the layer. Recrystallization of the wax immediately adjacent to the layer due to 'contact metamorphism' may lead to larger grainsizes and different rheological behaviour.

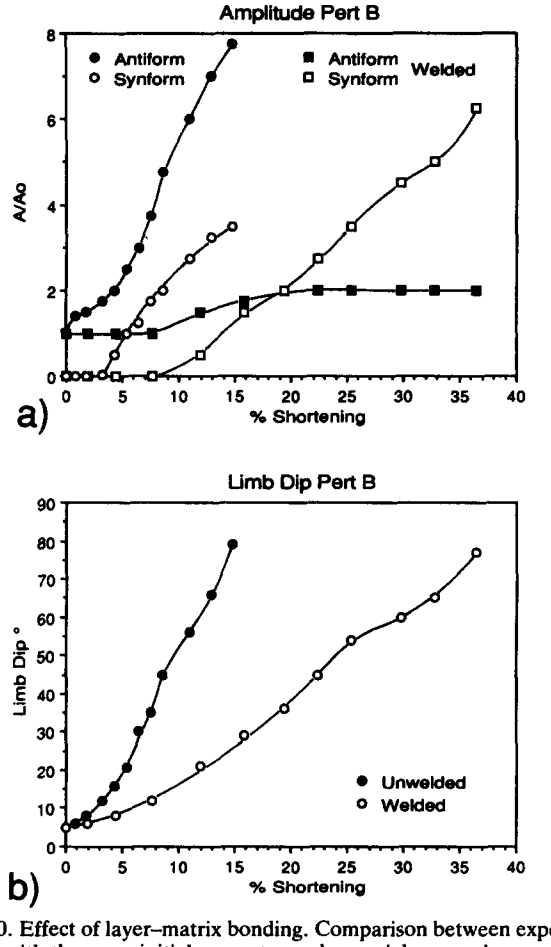

Fig. 20. Effect of layer–matrix bonding. Comparison between experiments with the same initial geometry and material properties, except that the contact was either welded or free to slip. (a) Normalized amplitude A/A_0 vs percentage bulk shortening of the model for the initial central antiform and for the flanking synforms which develop during progressive folding. (b) Limb dip (in degrees) vs percentage bulk shortening.

Influence of viscosity contrast

As expected from theoretical considerations and earlier scale model studies (e.g. Hudleston 1973), the

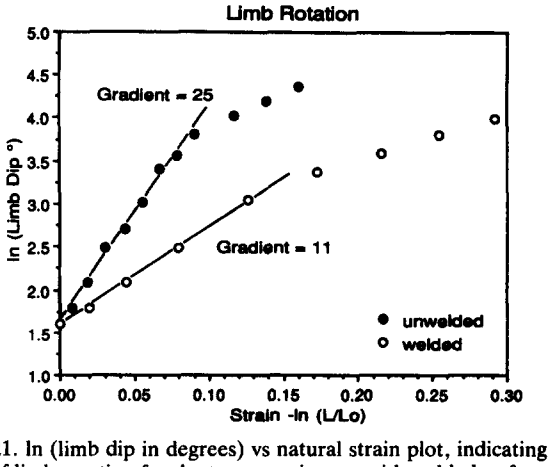

Fig. 21. ln (limb dip in degrees) vs natural strain plot, indicating the rate of limb rotation for the two experiments with welded or free-slip contacts, and emphasizing the significant influence of the degree of bonding.

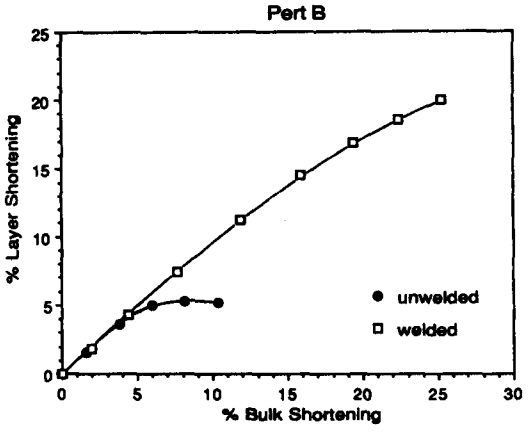

Fig. 22. Plot of layer parallel shortening against bulk shortening for the welded and unwelded contacts. Note the far greater layer parallel shortening undergone in the experiment with welded contacts.

experiment in which the viscosity contrast was only around 8:1 shows a much lower growth rate for the central antiform and much greater layer parallel shortening compared to the higher viscosity ratio experiments with similar initial perturbation geometry (Figs. 23–26). At high values of bulk shortening and layer parallel shortening, there is a progressive development of additional small 'folds' independent of the central initial perturbation. In three dimensions, on the surface of the layer, these are seen to be distinctly non-cylindrical (Fig. 8), probably reflecting the amplification of (unintentional) small irregularities distributed unevenly across the layer, as well as the effects of uneven friction on the upper and lower surfaces of the model. As the transfer of shortening from one non-cylindrical fold to another involves additional strains within the layer, it is reasonable to expect such geometries will become more significant at lower viscosity contrast between layer and matrix, as is observed in our experiments.

Hinge and inflection points

At very low fold amplitudes during the process of wavelength selection, hinge rolling and displacement of the inflection points through material points within the layer may occur (e.g. Chapple 1968). Once the folding is sufficiently advanced that these positions can be measured from the photographs with any confidence, however, their position remains effectively fixed to the same material points during subsequent fold amplification.

Finite strain distribution

For a viscosity contrast of 30:1 and unwelded easy-slip contacts between matrix and layer, the strain within the layer closely approximates that for tangential longitudinal strain (fig. 7-63 of Ramsay 1967). The lines of the initially rectangular grid, which were inscribed parallel and perpendicular to the layer boundary, remain parallel to the infinitesimal stretching axes throughout the deformation and, therefore, maintain the original 90° angles between the grid lines (Fig. 9). The finite strain axes within the layer thus remain perpendicular or parallel to the layer–matrix interface, leading to a strong refraction of the strain trajectories across this interface and the development of a low strain triangular zone on the outer arc of the folds (Fig. 27a). This spinning coaxial deformation history is to be expected (Lister & Williams 1983), since the easy-slip interface cannot support a shear stress and effectively functions as a free boundary. From the point of view of the stiff layer, the interface will also approximate a free boundary when viscosity contrasts between layer and matrix are high. The shear stress which can be supported in the weak matrix adjacent to the layer is, in this case, insignificant compared to the viscosity of the layer itself, and will produce only negligible shear strain rates within the

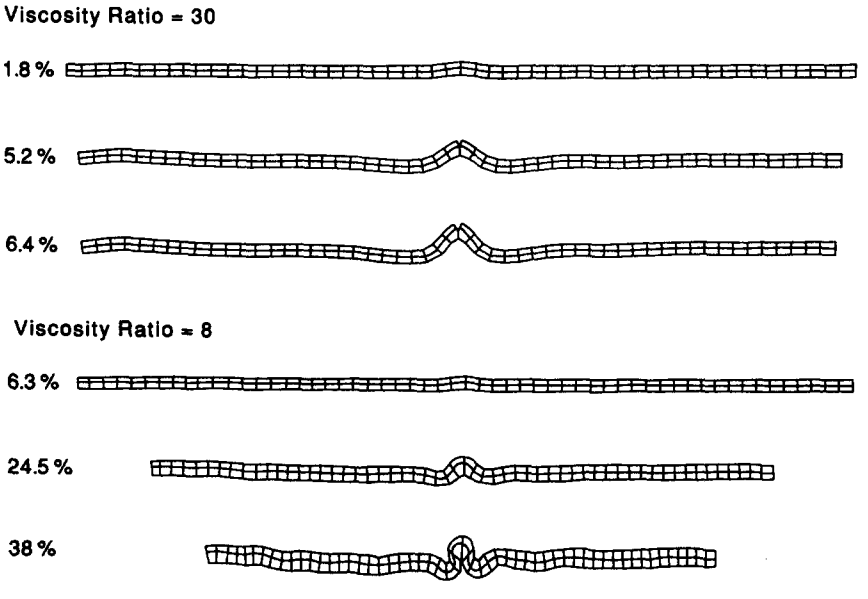

Fig. 23. Fold geometry developed in a single layer with an initial perturbation geometry similar to Pert A, but with only half the initial central perturbation amplitude, for two different viscosity ratios between layer and matrix (30:1 and 8:1).

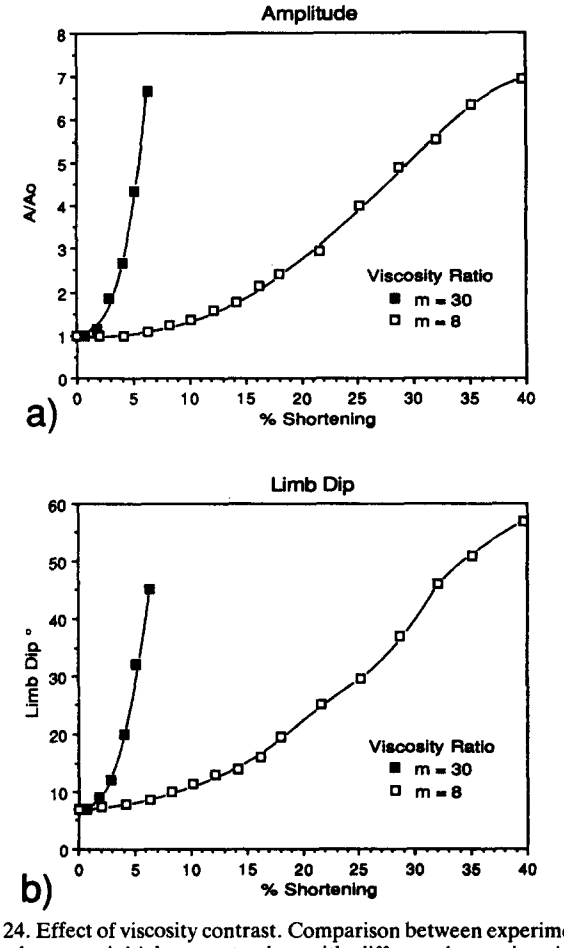

Fig. 24. Effect of viscosity contrast. Comparison between experiments with the same initial geometry but with different layer viscosities. (a) Normalized amplitude A/A_0 vs percentage bulk shortening of the model for the central antiform. (b) Limb dip vs bulk shortening.

layer parallel to the layer boundary. The distinction between easy-slip and welded boundaries should, therefore, become less important at high viscosity ratios between layer and matrix (cf. fig. 5 in Part II, Mancktelow & Abbassi 1992). In contrast, for welded contacts and low to moderate viscosity ratios (<50), where a significant shear stress can be transmitted across the interface, there is a more important component of layer parallel shear, the lines of the grid do not remain perpendicular, and refraction of the strain trajectories is

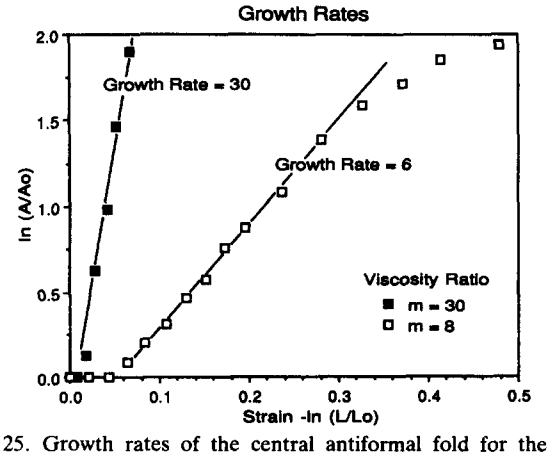

Fig. 25. Growth rates of the central antiformal fold for the two viscosity ratios.

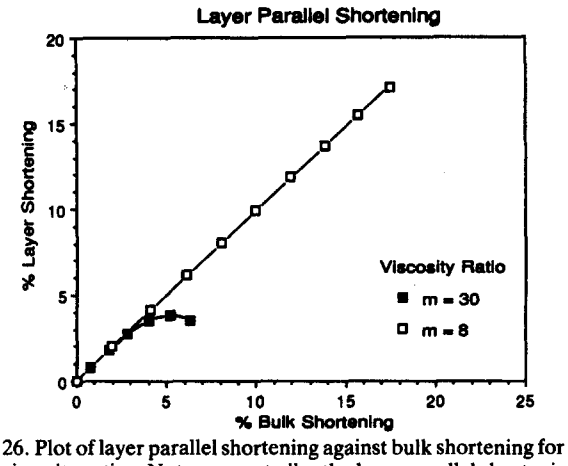

Fig. 26. Plot of layer parallel shortening against bulk shortening for the two viscosity ratios. Not unexpectedly, the layer parallel shortening is much greater in the experiment with low viscosity contrast.

less marked (Figs. 19 and 27b). This effect is even more strongly developed at very low viscosity contrasts (e.g. only 8:1 in Figs. 23 and 27c).

DISCUSSION

Fold geometry

At low amplitudes and limb dips, the assumption of independent and constant growth for each of the Fourier components comprising the fold form is valid to a good first-order approximation (e.g. Chapple 1968; fig. 7 in Part II, Mancktelow & Abbassi 1992). Folding can then be treated as the imposition of a single growth rate curve, as determined by the material properties, on the original amplitude distribution of components present in the initial perturbation shape. This approach is followed in Fig. 28, where the theoretical growth rate curve (Fig. 28a) was calculated using the equation derived independently by Fletcher (1974) and Smith (1979), with material properties such that the maximum growth rate occurs at $L_d/h = 10$ (or $h/L_d = 0.1$), where L_d is the 'dominant wavelength'. These growth rates were then applied to bell-shaped perturbations with average wavelengths of $1/2L_d$, L_d and $2L_d$, for logarithmic strains of $\varepsilon = -0.05$ and -0.10, and the results plotted in Figs. 28(b)–(d). In all cases, the wavelength component of maximum amplitude is longer than the 'dominant wavelength' of maximum growth rate, L_d, with the difference decreasing with increasing amplification.

As can be seen from plots of the maximum amplitude wavelength component vs strain in Fig. 29(a), the effect is most marked for broad initial perturbations (larger average wavelength L_{av}), but it is still seen for the perturbation with an initial average wavelength of only $0.5L_d$ ($L_{av} = 5$). This is because the amplitude of the components in an isolated bell-shaped perturbation decrease exponentially with decreasing wavelength, with the maximum amplitude at infinite wavelength (wavenumber $h/L = 0$). The components on the long wavelength side of the average wavelength will always be of

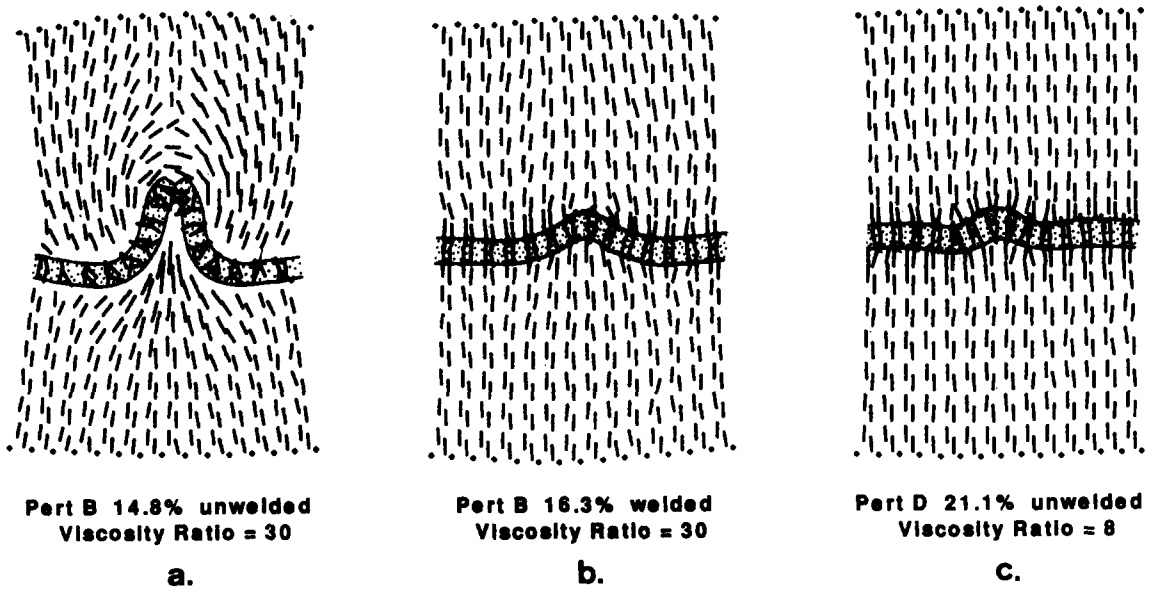

Fig. 27. Plot of the long axis of the finite strain ellipse across the upper surface of the model. (a) Pert B, easy-slip layer–matrix interface, viscosity ratio ≈30. (b) Pert B, welded layer–matrix interface, viscosity ratio ≈30. (c) Pert D, easy-slip layer–matrix interface, viscosity ratio ≈8.

greater amplitude, and will, therefore, always tend to shift the position of the maximum amplitude component in the fold packet towards the long wavelength side. The curves in Fig. 29 tend to be asymptotic, such that even at large total amplifications (high strain in Fig. 29a, high viscosity ratio in Fig. 29b), the influence of the initial perturbation on the final shape is never entirely eliminated. This is particularly noticeable when the initial perturbation was broad compared to the dominant wavelength. The theoretical curves of Fig. 29 also indicate that, for low total amplification, the maximum amplitude wavelength component always tends to infinity, which is the maximum amplitude component in the initial isolated perturbation. The theoretical dynamic fold growth rates in Fig. 28(a) are always positive and tend to zero for infinite wavelength (i.e. $h/L = 0$), such that the total growth rate approaches the kinematic value of 1. Long wavelengths will, therefore, also amplify during folding, but much more slowly than those wavelengths close to the dominant wavelength, and it will require a certain finite amplification before the original exponential distribution is overwhelmed and a new peak away from $h/L = 0$ develops (e.g. Figs. 28d and 29). Fourier analysis of the model experiments, as summarized in Figs. 13 and 14, produces results which differ somewhat from these theoretical predictions. Negative growth rates at very long wavelengths ($h/L \rightarrow 0$) are observed (i.e. amplitude *decreases* with increasing strain, cf. Smith 1979), resulting in a more rapid suppression of the long wavelength components and a correspondingly more rapid development of a separate peak at shorter wavelength. This peak itself, however, behaves as predicted from Fig. 29: its position changes little with increasing strain, particularly for broad initial perturbation shapes (reflecting the asymptotic behaviour of the curves in Fig. 29a), it is always developed at a longer wavelength than the expected dominant wavelength, and its position occurs at longer wavelengths for broader initial perturbations.

The amplified Fourier components can be used to construct the form of the theoretical fold shape for direct comparison with the observed shape (Part II, Mancktelow & Abbassi 1992), and thus also to determine the growth rate of the central antiform of the fold packet (Fig. 10) (Biot *et al.* 1961). A plot of this growth rate for various average wavelengths L_{av} of the initial perturbation is given in Fig. 30, using material properties similar to those of our experiments. For these specific properties, the dominant wavelength is 8.3 times layer thickness and the maximum growth rate associated with this wavelength is 27.8. From Fig. 30, it is immediately obvious that the growth rate of the central antiform will be a function of the initial perturbation shape. The maximum growth rate is considerably less than that of the dominant wavelength, and occurs for a L_{av} value slightly less than the dominant wavelength. For still shorter L_{av}, the growth rate of the central antiform decreases rapidly, for larger values it decreases more steadily. This effect can be understood by studying Fig. 28, comparing the growth rate curve (a) with the initial perturbation distributions (b)–(d). For very broad perturbations (e.g. d), most of the initial components lie to the left of the maximum growth rate (in this case, at layer thickness/wavelength = 0.1) and are therefore amplified more slowly than the maximum rate. For narrower perturbations (e.g. b and c), the initial curve spreads to shorter wavelengths and more components lie within the high growth rate band, leading to a higher overall growth rate for the perturbation but never attaining the maximum growth rate possible for a sinusoidal wave. If the perturbation becomes too narrow, however, more and more of the components will lie to the right (i.e. the

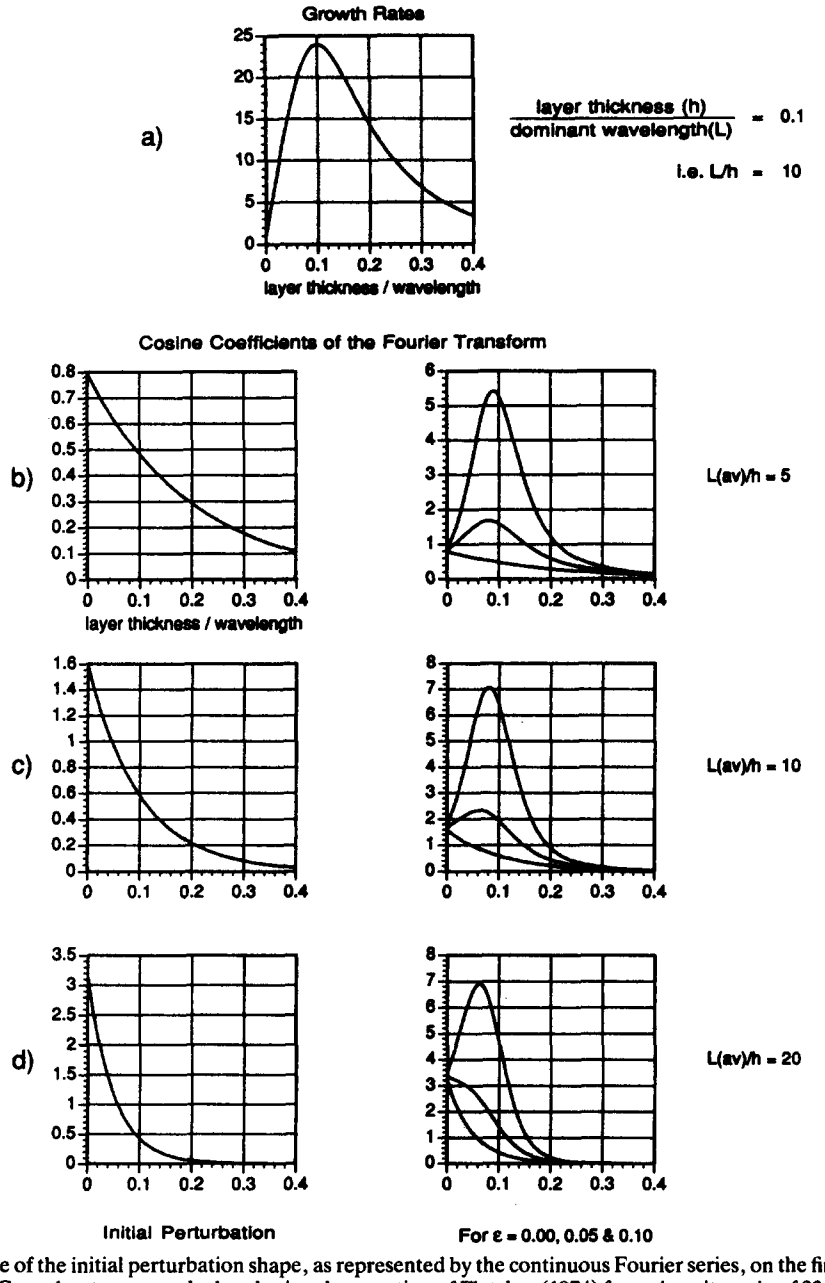

Fig. 28. Influence of the initial perturbation shape, as represented by the continuous Fourier series, on the final shape of the fold packet. (a) Growth rate curve calculated using the equation of Fletcher (1974) for a viscosity ratio of 33:1 and effective stress exponents in the layer and matrix of 3, producing a dominant wavelength of 10 times layer thickness (layer thickness/wavelength = 0.1). (b) Cosine coefficients of the Fourier series for a bell-shaped curve with initial average wavelength of 5 times layer thickness (left side) and after amplification by the growth rate curve in (a) at natural strains of 0.00 (initial form again), 0.05 and 0.10. (c) Same as (b), except that the initial average wavelength for the bell-shaped curve is 10 times layer thickness. (d) Same as (b), except that the initial average wavelength for the bell-shaped curve is 20 times layer thickness.

short wavelength side) of the maximum growth rate, and the growth rate of the perturbation will diminish rapidly as is indeed seen in Fig. 30.

Layer parallel shortening

At very low fold limb dips, the layer is everywhere effectively parallel to the principal shortening axis x_1, and the strain rate $\dot{\varepsilon}_{11}^{L}$ in the layer must be approximately equal to the strain rate imposed at the boundaries, i.e. $\dot{\varepsilon}_{11}^{L}/\dot{\varepsilon}_{11} \approx 1$ (e.g. Hudleston 1973, 1986). As the limbs rotate due to the buckling instability, less shortening occurs in the layer than in the surrounding matrix or is applied at the boundaries i.e. $\dot{\varepsilon}_{11}^{L}/\dot{\varepsilon}_{11} < 1$. This is the basic driving mechanism for buckle folding, namely the preferential partitioning of strain from the stiffer layer into the weaker matrix; if $\dot{\varepsilon}_{11}^{L}/\dot{\varepsilon}_{11}$ remained = 1, there could be no buckling instability, only kinematic amplification due to homogeneous strain.

Eventually, at limb dips of around 30–40°, layer parallel shortening effectively ceases (Fig. 15c). As the different initial geometries attain this 30–40° limb dip value at different values of bulk shortening, the maximum layer parallel shortening attained is different from one perturbation shape to another. The narrow perturbation Pert A, with an initial limb dip of 12° is shortened less than 4%, whereas the broadest perturbation Pert C, with an initial limb dip of 3°, reaches a maximum value of 6.5–

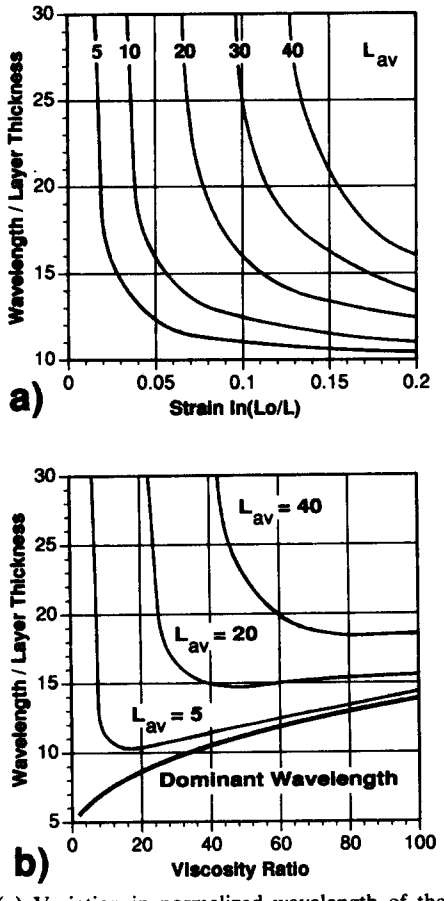

Fig. 29. (a) Variation in normalized wavelength of the maximum amplitude component of the Fourier series with increasing strain, for various values of average wavelength of the initial perturbation. Material properties are the same as Fig. 28 (viscosity ratio = 33, stress exponent of both layer and matrix = 3), which results in a theoretical dominant wavelength of 10 (cf. Fig. 28a). (b) Variation in normalized wavelength of the maximum amplitude component of the Fourier series with increasing viscosity ratio between layer and matrix, for various values of average wavelength of the initial perturbation, at a strain $\varepsilon = 0.10$. The dominant wavelength value is indicated by the lower thick curve.

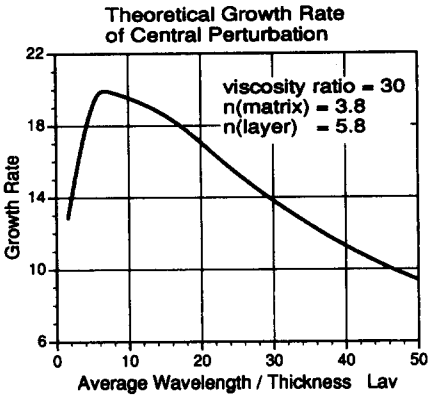

Fig. 30. Theoretical growth rate of the central antiform as a function of initial average wavelength of the perturbation L_{av}, using the theoretical growth rate equation of Fletcher (1974) for non-linear materials and the method of Biot *et al.* (1961). See Part II (Mancktelow & Abbassi 1992) for a summary of the technique.

7% layer parallel shortening. This consistent increase in the importance of layer parallel shortening with perturbation width is qualitatively predictable from equation (7) of Ramberg (1964), which indicates that, for any specific (linear viscous) material properties and a regular sinusoidal fold form, the ratio of shortening due to buckling relative to homogeneous layer parallel shortening will be directly proportional to $(A/L)^2$, where A is the amplitude and L the wavelength of the fold. Broader initial perturbations with longer average wavelength should, therefore, experience more layer parallel shortening than narrower perturbations of the same amplitude, as is indeed observed in the experiments.

As the folds amplify further, limb dips can exceed 45°, placing them in the field of incremental extension for the basic flow, such that extension in the limbs can counteract continued shortening in the hinges. As the dynamic amplification decreases (Fig. 10b), continued kinematic amplification will eventually produce hinge thickening and limb thinning, leading to typical 'flattened parallel folds' approaching a similar-style geometry (e.g. Ramsay 1967, p. 411) and resulting in a progressive increase in the total arc length measured along the folded layer.

Not only the shape, but also the spacing of initial perturbations may influence the amount of layer parallel shortening which accompanies folding. As has been observed in both current experiments and in those of Cobbold (1975), the location of fold packets is determined by the location of the initial perturbations. If perturbations are closely spaced, folding can initiate at many sites simultaneously and much of the total shortening can be accommodated by buckling. In contrast, if the perturbations are very widely spaced, there are few fold initiation sites, and shortening in the layer must be transferred over considerable distances if it is to be accommodated by buckling. As discussed in more detail below, the degree of bonding between layer and matrix will then become crucial in determining if shortening is accommodated locally by layer parallel shortening or if it is transferred to sites of isolated folding by relative slip along the layer–matrix interface.

Sherwin & Chapple (1968) developed an extension of the theoretical analysis of Biot (1961, 1965) to include the effects of layer parallel shortening. They implicitly assumed, however, that the strain rate in the layer and matrix remain the same during folding to finite amplitudes, i.e. $\dot{\varepsilon}_{11}^{L} = \dot{\varepsilon}_{11}$. As discussed above, this is only instantaneously true at fold initiation (Fig. 15). In general, as noted by Biot (1965, pp. 425–428), finite strain will result in a shortening of wavelengths (related to the strain rate of the basic flow parallel to the layer $\dot{\varepsilon}_{11}$, as applied at the model boundaries) and a thickening of the layer itself (related only to the layer parallel shortening component $\dot{\varepsilon}_{11}^{L}$). As can be seen from Fig. 15, the layer parallel shortening is a function of the bulk shortening $\varepsilon_{11}^{L} = f(\varepsilon_{11})$. If this function is known and sufficiently simple, an analytical solution for amplification vs wavelength may be possible. Usually, a numerical solution is required. Such a numerical solution, which includes layer parallel shortening as measured experimentally (e.g. Fig. 15), is discussed in Part II (Mancktelow & Abbassi 1992). These results confirm the observation of Biot (1965, p. 427) that the effects of layer thickening

and wavelength shortening tend to counteract one another and that the influence of these finite strain effects on the low-limb dip fold geometry is not great. However, continued layer parallel shortening to large finite values, such as are typical of folding with low viscosity contrast between layer and matrix (cf. Fig. 26), will eventually modify fold shapes to characteristic cuspate–lobate forms (e.g. Ramsay & Huber 1987, fig. 19.14).

Layer–matrix bonding

The experimental results show a strong dependence of fold development on the degree of bonding between layer and matrix. For the easy-slip experiments, shortening accrues largely by buckle folding with only a minor, though significant, component of layer parallel shortening. The buckling component, however, is restricted to the central region around the initial perturbation and is not evenly distributed along the layer. Detachment between layer and matrix along the easy-slip interface allows a transfer of shortening to this central region, much as detachments in nature allow transfer of strain from one location to another (e.g. low-angle decollément). The outer segments of the layer away from the central perturbation are driven in as straight 'pile drivers' towards the central region, where the shortening of the layer as a whole is accommodated locally by buckling. If the rate of bulk shortening cannot be fully accommodated by buckling with a growth rate as determined by the material properties, then the additional strain must be accommodated by layer parallel shortening.

The hinge point of maximum amplitude of the perturbation (cf. Fig. 5) does not slip relative to the adjacent matrix. It acts as a pin point, or 'spot weld' along the layer, preventing further transfer of shortening along the detachment and thus concentrating the buckling strain about this point. By analogy, it is clear that variation in the degree of bonding along a layer may also act as an irregularity leading to fold nucleation. If the initial irregularities are widely spaced, the amount of shortening transferred to each fold packet from the adjacent, detached, planar layer will be large. There will be a strong spatial variation along the layer in the amount of shortening accommodated by buckling and a corresponding spatial variation in the perturbation strain in the adjacent matrix (Fig. 16). If perturbations are closely spaced, the transfer will occur over a smaller distance and the total shortening of the layer will be accommodated more homogeneously. If the spacing is very close, then all the shortening can be accommodated locally and there will be little transfer of strain along the layer. As each hinge acts as a pin point, it is clear that for closer and closer spacing, the distinction between well-bonded and free-slip boundaries is reduced and may become insignificant: this is the geometry considered by Biot (1959) and Smith (1975), who showed theoretically that, in this case, the difference in behaviour between free-slip and no-slip boundaries should not be large and should become insignificant at higher viscosity contrasts (cf. fig. 5 in Part II, Mancktelow & Abbassi 1992).

It follows that, for low to moderate viscosity contrasts between layer and matrix, there will be an interrelation between the degree of bonding, the spacing of initial perturbations, and the amount of layer parallel shortening. If the degree of bonding is very high, no transfer is possible and perturbation amplification is completely local and driven by the strain rate of the bulk deformation. In regions where the initial perturbation amplitudes were small and limb dips correspondingly low, the strain must be accommodated largely by layer parallel shortening (see Fig. 15b). If the degree of bonding is very weak, the shortening of the layer can be transferred by displacement of the layer relative to the matrix, with detachments occurring to either side of the layer (i.e. layer parallel slip). The growth rate of individual fold packets will then depend to some extent on the spacing of the larger irregularities.

The degree of bonding between matrix and layer may increase with increase in metamorphic grade, as crystallization of new mineral phases and grain growth act to weld layer boundaries. Certainly the best examples of flexural slip folding, involving discrete slip between layers, are known from low metamorphic grade regions (e.g. Tanner 1989). This tendency to increased welding of contacts, and its corresponding influence on growth rates and layer parallel shortening during folding, may be one factor in explaining the preponderance of cuspate–lobate fold geometries, indicative of low growth rates and significant layer parallel shortening, in moderate to high metamorphic grade terrains (e.g. fig. 19.16 from Ramsay & Huber 1987).

Comparison with a sinusoidal fold of constant arc length

Several features of the finite-amplitude folding observed in the experiments can be effectively discussed by comparison with the geometry of a sinusoidal of constant arc length. From the curves in Fig. 31, it is seen that the initial amplification rate of such a sinusoidal fold is infinite, but decreases rapidly as the limbs rotate with increased shortening. The amplification rate due to buckling instability is, however, always finite. It follows, as noted from the experiments discussed above, that the layer must initially undergo layer parallel shortening at the same rate as that imposed on the boundaries (Fig. 15b). The layer parallel shortening will decrease rapidly with increasing limb dip until the growth rate of the buckling instability and that required for constant length amplification instantaneously coincide. In the next infinitesimal strain increment, buckling can occur at constant arc length. Further amplification must either involve an increase in arc length, or the growth rate of the fold must progressively decrease to mimic that of a constant arc length fold (a finite strain effect, as is indeed seen in Fig. 10b). As the growth rate due to buckling is lower for lower viscosity contrast, low viscosity contrast folds will obviously experience more layer parallel short-

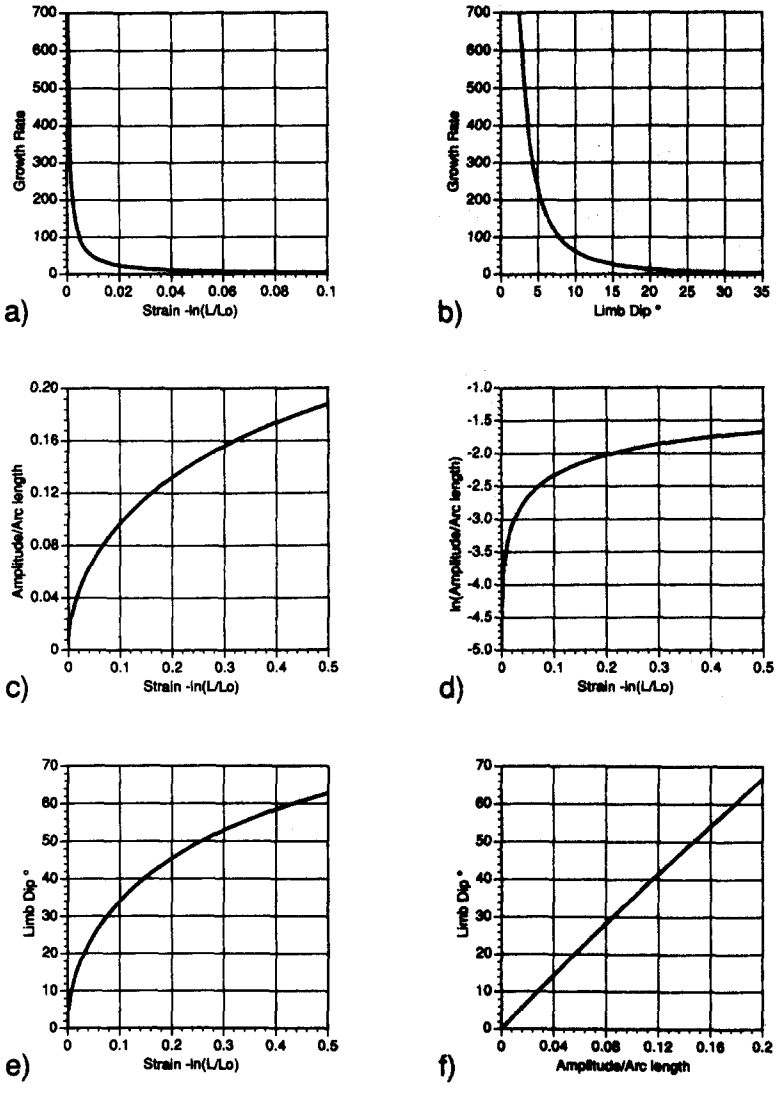

Fig. 31. Parameters calculated for buckling of a sinusoidal wave of constant arc length. Initial amplitude is zero and arc length is 2π. To non-dimensionalize the result, amplitude is normalized against this constant arc length. (a) Growth rate ($\partial(\ln(\text{amplitude/arc length}))/\partial\varepsilon$) vs $-$logarithmic strain ε. (b) Growth rate vs maximum limb dip (in degrees). (c) Normalized amplitude vs $-$logarithmic strain. (d) ln (normalized amplitude) vs $-$logarithmic strain. The slope of this curve at every point gives the value of the growth rate plotted in (a). (e) Limb dip (in degrees) vs $-$logarithmic strain. (f) Limb dip (in degrees) vs normalized amplitude. Note the relationship is practically linear within the plotted range.

ening before this critical cross-over point is reached than high viscosity contrast folds. Broad initial perturbations with lower initial limb dips will also take longer to pass this cross-over point and should, therefore, experience more layer parallel shortening than narrow perturbations with higher initial limb dips (Fig. 15).

For a sinusoidal curve of constant arc length, there is a nearly linear relationship between maximum limb dip at the inflection point and amplitude up to quite high limb dips (Fig. 31f). This linear relationship is also seen in the experiments (Fig. 12).

CONCLUSIONS

The experiments confirm that the presence of an initial isolated perturbation in a single layer not only controls the location of the developing fold packet but also exerts an important influence on the geometry of developing folds (e.g. Willis 1893, Hobbs 1914, Biot *et al.* 1961, Cobbold 1975, Lewis & Williams 1978, Williams *et al.* 1978). For isolated and non-periodic initial perturbations, folding spreads sideways along the layer away from the position of maximum amplitude of the initial irregularity. Parameters such as the amount of layer parallel shortening, the growth rate of the central fold, the maximum amplitude component to the fold train and the symmetry (Abbassi & Mancktelow 1990) are all affected by the shape of the initial perturbation. For the same initial amplitude, broader perturbations with lower initial limb dip show a slower growth rate and correspondingly greater layer parallel shortening. In the extreme, the growth rate of a very broad perturbation with very low limb dip must approach zero, and all shortening will be accommodated by homogeneous layer parallel shortening (e.g. Smith 1975).

Most of the experimental-scale models were constructed such that slip between layer and matrix was

promoted, but in one particular series this interface was welded. Folds in the welded experiments grew much more slowly, with correspondingly more layer parallel shortening. These preliminary results, which still need to be fully tested on a wider range of analogue materials, suggest that the degree of bonding across the interface between layer and matrix may have an important influence on fold geometry at low to moderate viscosity ratios (such as are predicted from the rather short wavelengths of many natural folds, e.g. table 1 from Smith 1979). If easy-slip is possible, shortening can be transferred to isolated folding sites by slip along the interface. If slip is not possible, the shortening in the layer must be accommodated locally, either by folding or by layer parallel shortening, with the relative importance determined not only by material properties but also by the geometry of local irregularities.

The initial perturbations considered in this series of experiments and in the theoretical treatment of buckle folding are taken to affect the whole layer, with identical shapes for both layer surfaces. Such an initial geometry may be expected in extensional veins, for example, where the two sides of the vein should match. It will not be the rule for sedimentary layers, where many initial irregularities affect one surface only (e.g. ripple marks, load casts, channels). The influence of such common irregularities on finite fold shape remain to be investigated in a further study.

Acknowledgements—Thorough reviews by Peter Cobbold, Raymond Fletcher and Sue Treagus greatly helped to improve the organization and presentation of the present paper, and were much appreciated. Thanks are due to John Ramsay for his support for the model deformation laboratory, to Robert Hofmann for invaluable expertise in constructing the deformation rig, and to Martin Casey for many stimulating discussions on buckle fold mechanisms.

REFERENCES

Abbassi, M. R. & Mancktelow, N. S. 1990. The effect of initial perturbation shape and symmetry on fold development. *J. Struct. Geol.* **12**, 273–282.

Biot, M. A. 1959. On the instability and folding deformation of a layered viscoelastic medium in compression. *J. appl. Mech.* **E26**, 393–400.

Biot, M. A. 1961. Theory of folding of stratified viscoelastic media and its implications in tectonics and orogenesis. *Bull. geol. Soc. Am.* **72**, 1595–1620.

Biot, M. A. 1965. *Mechanics of Incremental Deformations*. John Wiley & Sons, New York.

Biot, M. A., Odé, H. & Roever, W. L. 1961. Experimental verification of the theory of folding of stratified viscoelastic media. *Bull. geol. Soc. Am.* **72**, 1621–1632.

Chapple, W. M. 1968. A mathematical theory of finite-amplitude rock-folding. *Bull. geol. Soc. Am.* **79**, 47–68.

Cobbold, P. R. 1975. Fold propagation in single embedded layers. *Tectonophysics* **27**, 333–351.

Fletcher, R. C. 1974. Wavelength selection in the folding of a single layer with power-law rheology. *Am. J. Sci.* **274**, 1029–1043.

Fletcher, R. C. & Sherwin, J. 1978. Arc lengths of single layer folds: a discussion of the comparison between theory and observation. *Am. J. Sci.* **278**, 1085–1098.

Hobbs, W. H. 1914. Mechanics of formation of arcuate mountains. Part II. *J. Geol.* **22**, 166–168.

Hudleston, P. J. 1973. An analysis of 'single layer' folds developed experimentally in viscous media. *Tectonophysics* **16**, 189–214.

Hudleston, P. J. 1986. Extracting information from folds in rocks. *J. Geol. Educ.* **34**, 237–245.

Hudleston, P. J. & Holst, T. B. 1984. Strain analysis and fold shape in a limestone layer and implications for layer rheology. *Tectonophysics* **106**, 321–347.

Lewis, R. W. & Williams, J. R. 1978. A finite-element study of fold propagation in a viscous layer. *Tectonophysics* **44**, 263–283.

Lister, G. S. & Williams, P. F. 1983. The partitioning of deformation in flowing rock masses. *Tectonophysics* **92**, 1–33.

Mancktelow, N. S. 1988a. An automated machine for pure shear deformation of analogue materials in plane strain. *J. Struct. Geol.* **10**, 101–108.

Mancktelow, N. S. 1988b. The rheology of paraffin wax and its usefulness as an analogue for rocks. *Bull. geol. Instn. Univ. Uppsala* **14**, 181–193.

Mancktelow, N. S. 1991. The analysis of progressive deformation from an inscribed grid. *J. Struct. Geol.* **13**, 859–864.

Mancktelow, N. S. & Abbassi, M. R. 1992. Single layer buckle folding in non-linear materials—II. Comparison between theory and experiment. *J. Struct. Geol.* **13**, 105–120.

Neurath, C. & Smith, R. B. 1982. The effect of material properties on growth rates of folding and boudinage: experiments with wax models. *J. Struct. Geol.* **4**, 215–229.

Panozzo, R. 1988. Distortion of orientation data introduced by digitizing procedures. *J. Microscopy* **149**, 83–96.

Ramberg, H. 1961. Contact strain and folding instability of a multilayered body under compression. *Geol. Rdsch.* **51**, 405–439.

Ramberg, H. 1963. Fluid dynamics of viscous buckling applicable to folding of layered rocks. *Bull. Am. Ass. Petrol. Geol.* **47**, 484–505.

Ramberg, H. 1964. Selective buckling of composite layers with contrasted rheological properties. *Tectonophysics* **1**, 307–341.

Ramsay, J. G. 1967. *Folding and Fracturing of Rocks*. McGraw-Hill, New York.

Ramsay, J. G. & Huber, M. I. 1987. *The Techniques of Modern Structural Geology, Volume* 2: *Folds and Fractures*. Academic Press, London.

Sherwin, J. & Chapple, W. M. 1968. Wavelengths of single layer folds: a comparison between theory and observation. *Am. J. Sci.* **266**, 167–179.

Smith, R. B. 1975. Unified theory of the onset of folding, boudinage and mullion structure. *Bull. geol. Soc. Am.* **86**, 1601–1609.

Smith, R. B. 1979. The folding of a strongly non-Newtonian layer. *Am. J. Sci.* **279**, 272–287.

Suppe, J. & Medwedeff, D. A. 1990. Geometry and kinematics of fault-propagation folding. *Eclog. geol. Helv.* **83**, 409–454.

Tanner, P. W. G. 1989. The flexural-slip mechanism. *J. Struct. Geol.* **11**, 635–655.

Williams, J. R., Lewis, R. W. & Zienkiewicz, O. C. 1978. A finite-element analysis of the role of initial perturbations in the folding of a single viscous layer. *Tectonophysics* **45**, 187–200.

Willis, B. 1893. The mechanics of Appalachian structure. 13th Ann. Rep. U.S. Geol. Survey, Part II, 213–281.

APPENDIX

The limb dip α at the inflection point of a sinusoidal wave form is given by $\tan \alpha = 2\pi A/L$, where A is the amplitude and L the wavelength. Both numerical (e.g. Chapple 1968) and analogue models (e.g. Hudleston 1973) indicate that wavelength selection only occurs during the initial, low amplitude stages of buckle folding, and has effectively ceased by 15° limb dip. For $\alpha = 15°$, $\alpha \approx \tan \alpha$, and thus $15° \approx 360°\ A/L$, or $A \approx L/24$. If the amplification A/A_0 (A is the current amplitude, A_0 the initial perturbation amplitude) is to exceed 1000 before cessation of the wavelength selection process, then A_0 must be $\leq L/24{,}000$. Natural single layer fold wavelengths are generally less than 10 times the layer thickness, with common values in the range 4–8 (e.g. Sherwin & Chapple 1968, Smith 1979, Hudleston & Holst 1984). It follows that, for natural folds, the amplitude of shape perturbations in the layer must be less than around 1/2400 of the layer thickness if a well defined dominant wavelength is to be established which will be independent of the initial shape of the perturbations: i.e. <0.004 mm in a 1 cm layer or less than 0.4 mm in a 1 m thick layer.